INNOVATIONS IN THE FIELD OF ELECTRICAL-ELECTRONICS AND COMMUNICATIONS

Editor: İSHAK PARLAR

BİDGE

BİDGE Yayınları

Innovations in the Field of Electrical-electronics and Communications

Editor: İSHAK PARLAR

ISBN: 978-625-8995-19-0

1st Edition
Page Layout By: Gözde YÜCEL
Publication Date: 2026-03-25
BİDGE Yayınları

Certificate No: 71374

www.bidgeyayinlari.com.tr - bidgeyayinlari@gmail.com
Krc Bilişim Ticaret ve Organizasyon Ltd. Şti.
Güzeltepe Mahallesi Abidin Daver Sokak Sefer Apartmanı No: 7/9 Çankaya / Ankara

PREFACE

This book aims to bring together the rapid developments and innovative approaches in the fields of electrical-electronics and communication in recent years. In today's world, where technology is advancing at a dizzying pace, these fields are no longer limited to engineering disciplines but have become fundamental elements shaping every aspect of daily life.

The studies included in this work cover a wide range of current topics, from communication systems to smart devices, from artificial intelligence applications to next-generation electronic designs. The book aims to contribute to academic research and to serve as a guiding resource for professionals and students in the sector. We thank all the authors and contributors who contributed to the preparation of this work and hope that it will be a useful and inspiring resource for readers.

Assist. Prof. Dr. İshak PARLAR

CONTENTS

SVC-POD, TY MODEL VE YAKIT HÜCRESİ KULLANILARAK GÜÇ SİSTEMLERİNDE GEÇİCİ KARARLILIK DURUMLARININ İNCELENMESİ 1

MEHMET KENAN DÖŞOĞLU

ARTIFICIAL INTELLIGENCE AND ADVANCED DEEP LEARNING–BASED EARLY DIAGNOSIS AND INTERPRETATION/PRE-DIAGNOSIS OF PSYCHOLOGICAL DISORDERS USING ELECTROENCEPHALOGRAPHY (EEG) DATA 22

ALİ BERKAN URAL, MUHAMMED EMİN ÖZYILMAZ, HÜMEYRA KARADENİZ

SPIKING NEURAL NETWORKS: MODELS, COMPUTATION, AND SIMULATION TOOLS 43

İBRAHİM ÖZTÜRK

FLUX PINNING MECHANISMS OF SUPERCONDUCTING SAMPLES SUBSTITUTED WITH DIFFERENT RATIOS OF NANO-SIZED EU TO STRONTIUM SITES 60

MEHMET ERSİN AYTEKİN

CHAPTER 1

SVC-POD, TY MODEL VE YAKIT HÜCRESİ KULLANILARAK GÜÇ SİSTEMLERİNDE GEÇİCİ KARARLILIK DURUMLARININ İNCELENMESİ

BAYRAM PEKTAŞ [1]
M. KENAN DÖŞOĞLU [2]
ENES KAYMAZ [3]

Giriş

Dünya genelinde nüfus artışıyla birlikte enerjiye olan talep sürekli bir artış göstermektedir. Bu durum, güç sistemlerinin işletme koşullarında önemli değişimlere yol açmaktadır. Söz konusu değişimler, güç sistemlerinin dinamik davranışlarını etkileyerek çeşitli kararsızlık problemlerinin ortaya çıkmasına neden olmaktadır. Güç sistemlerinde meydana gelen bu kararsızlıkları gidermek amacıyla farklı yöntemler uygulanmaktadır. Bu yöntemlerden biri, güç elektroniği tabanlı Esnek AC İletim Sistemi (FACTS) elemanlarının kullanılmasıdır. FACTS cihazları arasında yer alan

---

[1] Öğrenci, Düzce Üniversitesi Lisansüstü Eğitim Enstitüsü, Elektrik Elektronik Mühendisliği, Orcid: -0009-0003-0424-140X

[2] Prof. Dr., Düzce Üniversitesi Mühendislik Fakültesi, Elektrik Elektronik Mühendisliği Bölümü, Orcid: -0001-8804-7070

[3] Dr. Öğr. Üyesi, Düzce Üniversitesi, Mühendislik Fakültesi, Elektrik Elektronik Mühendisliği Bölümü, Orcid:-0000-0002-4774-0773

Statik Var Kompanzatör (SVC), güç sistemleri kararlılık analizlerinde en yaygın kullanılan çözümlerden biri olarak öne çıkmaktadır. Literatürde SVC'ye yönelik çok sayıda çalışma bulunmaktadır.

Farklı çalışma koşullarında güç sistemlerinin bara gerilim profillerinin düzenlenmesinde SVC etkin bir rol oynamaktadır. Çok baralı güç sistemlerinde yüklenme parametrelerinin iyileştirilmesi ve bara gerilimlerinin işletme sınırları içerisinde kalmasının sağlanmasında SVC'nin katkısı oldukça büyüktür. Bunun yanı sıra, sürekli yük akışı analizlerinde yük baralarına ait gerilim seviyelerinin değişen işletme koşullarına bağlı olarak arttığı çeşitli çalışmalarda gösterilmiştir (Sode-Yome & Mithulananthan, 2004); (Bhole & Nigam, 2015); (Kamarposhti & Alinezhad, 2009). Farklı iletim açısı değerlerinde güç sistemlerinin reaktif güç taleplerinin karşılanmasında SVC'nin etkin ve yaygın bir çözüm sunduğu görülmektedir. Tristör tabanlı yapısından kaynaklanan harmonik bileşenlerin azaltılmasında SVC'nin önemli bir katkı sağladığı çeşitli çalışmalarda ifade edilmiştir (Sujatha, Anita, Selvan, & Selvakumar, 2015); (Thukaram, Khincha, & Ravikumar, 2004). Çok baralı güç sistemlerinde geçici kararlılık durumlarında, iletim sisteminin dinamik performansının iyileştirilmesi ve hızlı dinamik tepki elde edilmesinde tristör kontrollü reaktör ve tristör anahtarlamalı kapasitör birimlerinden oluşan SVC'nin etkili olduğu rapor edilmiştir. Bunun yanı sıra, sistem geriliminin düzenlenmesi ve bozucu etkilerin kontrol altına alınmasında SVC'nin hızlı bir denetim yapısına sahip olduğu gözlemlenmiştir (Rahim, Nowicki, & Malik, 2006); (Sabai, Maung, & Win, 2008). SVC'nin çok baralı güç sistemlerinde daha iyi bir dinamik performans sergilemesi amacıyla uygulanan yöntemlerden biri, denetleyici parametrelerinin optimum şekilde belirlenmesidir. SVC'de kullanılan PI denetleyici parametrelerinin tasarımında farklı optimizasyon ve ayarlama yaklaşımları geliştirilmiştir. Bu yöntemler sayesinde sistem kararsızlıklarının hızlı bir şekilde bastırıldığı ve kararsızlık durumlarında meydana gelen salınımların etkin biçimde sönümlendiği gösterilmiştir (Karpagam, Devaraj, & Subbaraj, 2010); (Wang, ve diğerleri, 2000); (Shaaban & Mesalam, 2022). Öte yandan, yenilenebilir enerji kaynaklarının sonsuz şebekeye entegrasyonu son yıllarda giderek önem kazanmaktadır. Özellikle rüzgar enerjisi dönüşüm sistemlerinde, rüzgar türbinlerinin şebeke entegrasyonu ve değişken çalışma koşullarına bağlı olarak ortaya çıkan geçici rejimlerin analizinde SVC yaygın bir şekilde kullanılmaktadır (Rezaie & Kazemi-Rahbar, 2019); (Uong & Ngamroo, 2015); (Ding, Meng, & Qiao, 2015). Seri kapasitörlerin kullanılması sonucu güç sistemlerinin aşırı kompanze edilmesi, alt senkron rezonans problemlerinin ortaya çıkmasına yol açmaktadır. Bu rezonans türlerinin giderilmesinde SVC yaygın olarak tercih edilen bir FACTS cihazıdır. İlgili çalışmalarda, SVC'nin SSR koşulları altında oluşan salınımları hızlı bir şekilde bastırdığı gösterilmiştir (Zhang & Xiao, 2009); (Liu, Xu, & Gao, 2001). Çok makinalı güç sistemlerinde senkron generatörlerin geçici kararlılık incelemelerinde, SVC modeli PSS ile koordineli olarak kullanılmıştır. Bu koordineli kontrol yapısı sayesinde sistemin geçici kararlılığının kısa sürede yeniden tesis edildiği ve sistem değişkenlerindeki salınımların etkin biçimde sönümlendiği rapor edilmiştir (Abido & Abdel-Magid, 2003a); (Abido & Abdel-Magid, 2003b); (Xu, 2012). Bunun yanı sıra, SVC'nin küçük sinyal kararlılığı analizlerinde de olumlu katkılar sağladığı, özellikle özdeğerlerin daha kararlı bölgelere taşınmasında etkili olduğu ilgili çalışmalarda belirtilmiştir (Dehgani, Hakimzadeh, Habibi, & Afroozi, 2014); (Khan, Meena, & Bhowmick, 2015); (Farsangi, Nezamabadi-Pour, Song, & Lee, 2007).

Bu çalışmada, SVC'nin güç sistemlerinde kararlılık analizlerindeki etkinliğini artırmak amacıyla POD, farklı türbin yöneticisi (TY) modelleri ve yakıt hücresi ile kullanılması hedeflenmiştir. SVC ile entegre edilen bu elemanların koordineli kontrolü gerçekleştirilmiş ve sistemin küçük sinyal kararlılığı analiz edilmiştir. Analizlerde; açısal hız, yük barası gerilimleri, senkron generatörlerin aktif ve reaktif güçleri ile özdeğerlerin gerçek ve sanal bileşenleri temel parametreler olarak ele alınmıştır. Küçük sinyal kararlılığı değerlendirmelerinde özdeğer yerleşimleri, salınım frekansları ve çalışma modları dikkate alınmış olup, elde edilen sonuçlar ayrıntılı bir şekilde yorumlanmıştır.

Statik Var Kompanzatör - Güç Salınım Sönümleyicisi

Güç sistemlerinde baraya paralel olarak bağlanan güç elektroniği tabanlı Statik Var Kompanzatörü (SVC), tristör kontrollü reaktör (TCR) ve tristör anahtarlamalı kapasitör (TSC) yapılarından oluşmaktadır. SVC'nin temel yapısı Şekil 1'de gösterilmiştir.

Şekil 1 SVC'nin temel yapısı

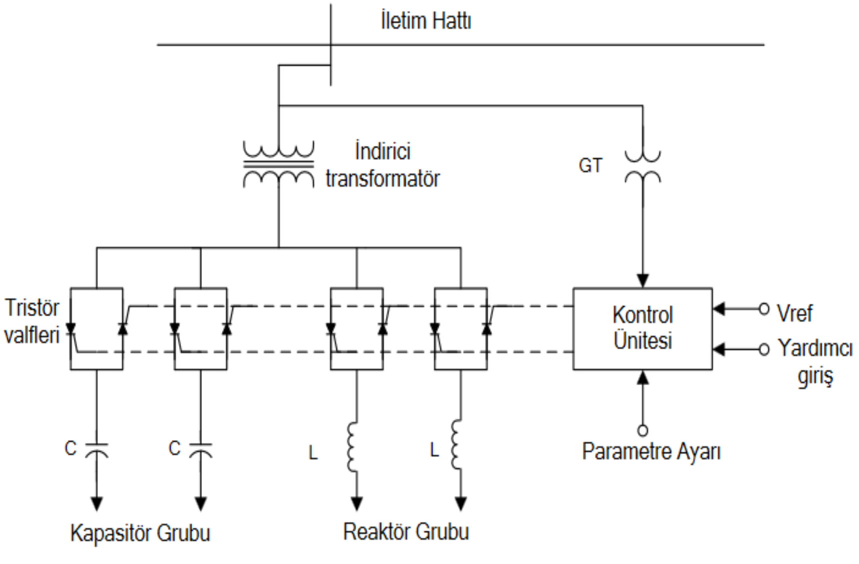

Şekil 1'de görüldüğü üzere SVC; kapasitör grupları, reaktör grupları, gerilim düşürücü transformatör ve kontrol ünitesinden oluşmaktadır. Bağlı bulunduğu baradaki akım ve gerilim bilgileri, sırasıyla akım ve gerilim transformatörleri aracılığıyla alınarak kontrol ünitesine iletilmektedir. Kontrol ünitesinde işlenen bu büyüklükler doğrultusunda, tristör kontrollü reaktör ve tristör anahtarlamalı kapasitör devrelerinde yer alan tristörler için uygun tetikleme açıları belirlenmektedir. SVC'nin eşdeğer süseptans ve reaktif güç ifadeleri Denklem (1) ve Denklem (2)'de sunulmuştur.

$$B_{SVC} = -\frac{1}{wL}(1-\frac{2\alpha}{\pi}) + wC \tag{1}$$

$$Q_{SVC} = -V_i^2 B_{SVC} \tag{2}$$

Burada, L ve C sırasıyla bobinin endüktansı ve kondansatörün kapasitans değerleridir. V_i SVC'nin bağlı olduğu baradır. α tristörlerin tetikleme açısıdır. Sistem yükü kapasitif olduğu durumda SVC sistemden reaktif güç tüketmek için tristör kontrollü reaktörü kullanır. Sistem yükü endüktif olduğu durumda SVC sisteme reaktif güç vermektedir (Ćalasan, Konjić, Kecojević, & Nikitović, 2020).

Güç Salınım Sönümleyicisi (POD), geçici kararlılık koşullarında ortaya çıkan salınımların kısa sürede sönümlenmesini sağlayan bir denetleyici yapıdır. POD modelinin blok diyagramı Şekil 2'de gösterilmiştir.

Şekil 2 POD modelinin blok diyagramı

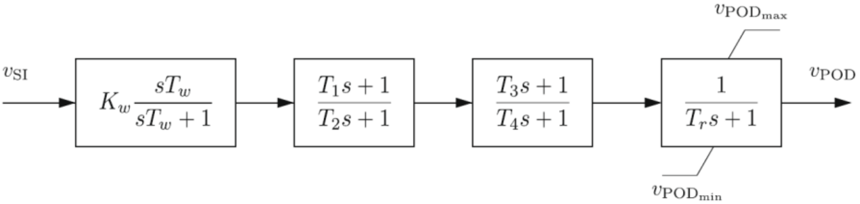

Şekil 2'de görüldüğü üzere POD transfer fonksiyonu; arındırma filtresi, dengeleyici kazanç ve faz kompanzatörlerinden oluşmaktadır. İstenen çıkış sinyali (V_{POD}) küçük bir zaman sabitine

(Tr) sahip filtre yardımıyla elde edilmektedir. Bu parametreler belirli sınırlar dâhilinde seçilebilmektedir. Uygun parametre değerlerinin belirlenmesiyle birlikte sönümleme kazancı (K_ω) en uygun seviyede ayarlanmaktadır. Bu yapı, SVC ile koordineli olarak kullanıldığında güç sistemlerinde meydana gelebilecek bozucu etkilere karşı etkin bir sönümleme performansı sunmaktadır (Ayres, Kopcak, Castro, Milano, & Costa, 2010); (Castro, Ayres, Da Costa, & Da Silva, 2007).

Senkron Generatörde Türbin Yönetici (TY) Modelleri

Senkron generatörlerde kullanılan denetleyicilerden biri olan türbin yöneticisi (TY), frekans kontrolü amacıyla kullanılmaktadır. Başka bir ifadeyle TY, moment sınırları ve sönümleme oranı dikkate alınarak güç ayarlamasını gerçekleştirmektedir. Sistem içerisinde mekanik momentin sınır değeri başlangıç aşamasında doğrulanmaktadır. Çalışmada iki farklı türbin yöneticisi modeli ele alınmıştır. TY-1 modeline ait matematiksel ifadeler Denklem (3)–(8) arasında verilmişken, TY-2 modelinin matematiksel gösterimi Denklem (9)–(11) arasında sunulmuştur.

$$p_{in}^{*} = p_{order} + \frac{1}{R}\left(\omega_{ref} - \omega\right) \tag{3}$$

$$p_{in} = \begin{cases} p_{in}^{*} & \text{if} \quad p^{\min} \le p_{in}^{*} \le p^{\max} \\ p^{\max} & \text{if} \quad p_{in}^{*} > p^{\max} \\ p^{\min} & \text{if} \quad p_{in}^{*} < p^{\min} \end{cases} \tag{4}$$

$$\dot{x}_{g1} = \left(p_{in} - x_{g1}\right) / T_s \tag{5}$$

$$\dot{x}_{g2} = \left(\left(1 - \frac{T_3}{T_c}\right) x_{g1} - x_{g2}\right) / T_c \tag{6}$$

$$\dot{x}_{g3} = \left(\left(1 - \frac{T_4}{T_5} \right) \left(x_{g2} + \frac{T_3}{T_c} x_{g1} \right) - x_{g3} \right) / T_5 \tag{7}$$

$$p_m = x_{g3} + \frac{T_4}{T_5} \left(x_{g2} + \frac{T_3}{T_c} x_{g1} \right) \tag{8}$$

$$\dot{x}_g = \left(\frac{1}{R} \left(1 - \frac{T_1}{T_2} \right) \left(\omega_{ref} - \omega \right) - x_g \right) / T_2 \tag{9}$$

$$p_m^* = x_g + \frac{1}{R} \frac{T_1}{T_2} \left(\omega_{ref} - \omega \right) + p_m^0 \tag{10}$$

$$p_m = \begin{cases} p_m^* & p^{\min} \leq p_m^* \leq p^{\max} \\ p^{\max} & p_m^* > p^{\max} \\ p^{\min} & p_m^* < p^{\min} \end{cases} \tag{11}$$

Burada ω_{ref} referans hız, p^{max} maksimum türbin çıkışı, p^{min} minimum türbin çıkışı, T_s yönetici zaman katsayısı, T_c servo zaman katsayısı, T_3 geçici kazanç zaman katsayısı, T_4 güç oranı zaman katsayısı, T_5 reheat zaman katsayısı, *u* bağlantı durumu olarak tanımlanmıştır (Milano, 2015).

TY-1 modelinde, referans açısal hız ile senkron generatörün işletme sırasında sahip olduğu açısal hız arasındaki fark, 1/R oranındaki bir kazanç ile çarpılarak bir sinyal elde edilmektedir. Bu sinyal, aktif güç ile toplanarak giriş gücü oluşturulmaktadır. TY-2 modelinde ise TY-1 modeline benzer şekilde, referans açısal hız ile generatörün anlık açısal hızı arasındaki fark 1/R kazancı ile çarpılmaktadır. Elde edilen sinyal transfer fonksiyonu bloğundan geçirildikten sonra mekanik güç ile toplanmakta ve böylece mekanik gücün işletme anındaki değeri hesaplanmaktadır.

Yakıt Hücresi

Yakıt hücreleri; yakıt işlemcisi, yakıt hücresi devresi ve güç bağlantı birimi olmak üzere üç temel bölümden oluşmaktadır. Güç işlemcisi, enerji dönüştürme işlemlerinin gerçekleştirildiği yapıyı temsil ederken, yakıt hücresi devresi elektrokimyasal süreçler sayesinde elektrik üretiminin sağlandığı bölümdür. Güç bağlantı birimi ise AC güç akımı, gerilim ve frekans bileşenlerini barındırmakta olup, şebekenin ihtiyaçlarına göre AC–DC güç dönüşümünü gerçekleştirmektedir. Bu birim iki ayrı bloktan meydana gelmektedir. İlk blok, aktif ve reaktif güç bilgilerini şebekeye ileten ve şebeke arayüz denetleyicisi olarak tanımlanan yapıdır. İkinci blokta ise yakıt hücresinin durağan modeli yer almakta olup, sistemdeki diğer alt birimlerin kararlı ve dengeli çalışmasını temin etmektedir. Genel olarak yakıt hücresinde aktif güç hesaplaması sayesinde akım ve modülasyon indeks değerleri hesaplanmaktadır. Bu değerlere bağlı olarak yakıt hücresine etkin eden aktif ve reaktif güç değerleri kolaylıkla hesaplanmaktadır (Yildirim & Gencoglu, 2018).

Küçük Sinyal Kararlılığı

Güç sistemleri çeşitli bozucu etkilere maruz kaldığında, sistemin küçük sinyal kararlılığını değerlendirmek amacıyla özdeğer analizleri gerçekleştirilmektedir. Özdeğerlerin hesaplanması Lyapunov'un birinci yöntemi temel alınarak yapılmaktadır. Benzetim çalışmaları sonucunda elde edilen özdeğerlerin gerçek kısımlarının negatif olması durumunda sistemin asimptotik olarak kararlı olduğu kabul edilmektedir. Buna karşılık, özdeğerlerden en az birinin gerçek kısmının pozitif olması sistemin kararsız olduğuna işaret etmektedir. Özdeğerlerin sanal kısımları sistemdeki salınım frekanslarını belirlemektedir. Karmaşık özdeğerler ise yerel alan ve bölgeler arası salınım modlarını temsil etmekte olup, eşlenik çiftler halinde ortaya çıkmaktadır. Bu eşlenik özdeğer çiftleri Denklem

(12)'de verilmiş, salınım frekansı ve sönüm oranları sırasıyla Denklem (13) ve Denklem (14)'te ifade edilmiştir (Mohammadpour & Santi, 2022); (Essallah, Bouallegue, & Khedher, 2019).

$$\lambda = \sigma \pm j\omega \tag{12}$$

$$\phi = \frac{\omega}{2\pi} \tag{13}$$

$$\zeta = \frac{-\sigma}{\sqrt{\sigma^2 + \omega^2}} \tag{14}$$

Denklem (12), (13) ve (14)'ten elde edilen sonuçlar doğrultusunda sistemin küçük sinyal kararlılığı analizleri gerçekleştirilmektedir. Bu çalışmada, farklı denetleyici modellerinin kullanılmasıyla elde edilen sonuçlar küçük sinyal kararlılığı açısından ayrıntılı bir şekilde değerlendirilmiştir.

Benzetim Çalışması ve Sonuçları

Bu çalışmada IEEE'nin 9 baralı güç sistemi kullanılmıştır. Bu benzetim çalışmasında Güç Sistemleri Analizi Programı (PSAT) kullanılmıştır (Milano F., 2005) . IEEE'nin 9 baralı güç sistemi Şekil 3'te verilmiştir. IEEE'nin 9 baralı güç sisteminde 1 tane salınım barası, 2 tane generatör barası ve 6 tane yük barası kullanılmıştır. 9 baralı sistemde 2-7 ve 3-9 numaralı baralar arasında transformatörler bulunmaktadır. Sistemde bulunan üç senkron generatörde otomatik gerilim regülatörleri ve 3. derece modelleri tercih edilmiştir. Otomatik gerilim regülatörlerinde model 3 kullanılmıştır. Bunun yanı sıra senkron generatörlerde TY model 1 ve TY model 2 analizler için tercih edilmiştir [16]. POD'un test sistemine yerleşim yeri olarak bara gerilim profilleri düşük olan 6 ve 9 numaralı baralarda POD'un yerleşimi yapılmıştır.

Şekil 3 9 baralı güç sistemi

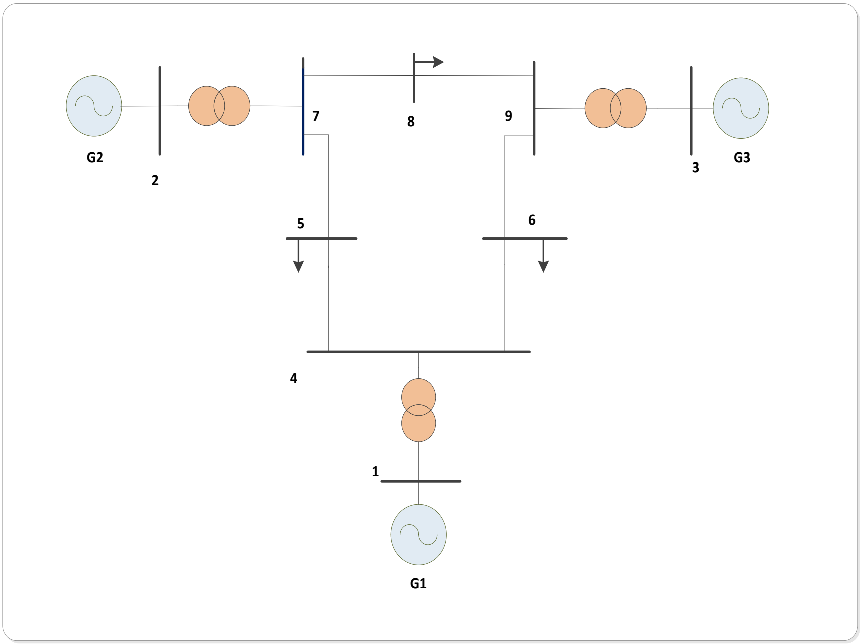

Sistemdeki geçici durum 5 ile 7 numaralı baralar arasındaki hatların 1 ile 1.1 saniyeler arasında devre dışı kalması olarak düzenlenmiştir. Senkron generatörde kullanılan TY 1 ve TY 2 modelin geçici kararlılık analizi öncelikle test edilmiştir. Sonuç olarak TY 2 modelin daha iyi sonuçlar verdiği ilgili çalışmada görülmüştür. Bundan yola çıkarak bu çalışma için TY 2 modelin kullanılması benimsenmiştir. İki analiz olarak çalışma gerçekleştirilmiştir. İlk analizde 100 MVA gücündeki SVC'nin 8 numaralı barada bağlı iken, senkron generatörde TY 2 model kullanıldığındaki sonuçlar irdelenirken, ikinci analizde 100 MVA gücündeki SVC'nin 8 numaralı barada bağlı iken, 3 numaralı barada 100 MVA gücündeki yakıt hücresinin kullanılması ve senkron generatörde TY 2 model kullanıldığındaki sonuçlar irdelenmiştir.

100 MVA gücündeki SVC'nin 8 numaralı barada bağlı iken, senkron generatörde TY 2 model kullanıldığındaki elde edilen

sonuçlar Şekil 4’te gösterilirken, birinci analizdeki gerçek-sanal değer sonuçları Şekil 5’te gösterilmiştir. Bunun yanı sıra birinci analizdeki 100 MVA gücündeki SVC’nin 8 numaralı barada bağlı iken, senkron generatörde TY 2 model kullanıldığındaki küçük sinyal kararlılığı sonuçları Tablo 1’de gösterilmiştir. İkinci analizde 100 MVA gücündeki SVC’nin 8 numaralı barada bağlı iken, 100 MVA gücündeki yakıt hücresi 3 numaralı baraya bağlı iken ve senkron generatörde TY 2 model kullanıldığındaki elde edilen sonuçlar Şekil 6’da gösterilirken, ikinci analizdeki gerçek-sanal değer sonuçları Şekil 7’de gösterilmiştir. Bunun yanı sıra ikinci analizdeki küçük sinyal kararlılığı sonuçları Tablo 2’de gösterilmiştir.

Şekil 4 SVC-POD, TY 2 model kullanıldığında elde edilen sonuçlar

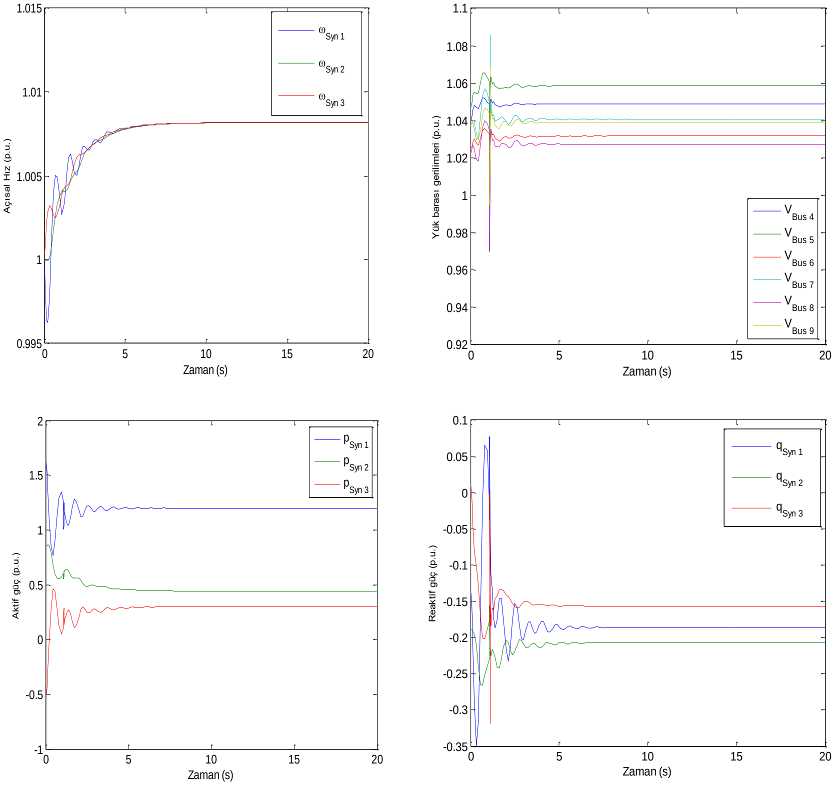

Şekil 5 SVC-POD, TY 2 model kullanımı ile gerçek-sanal değerler

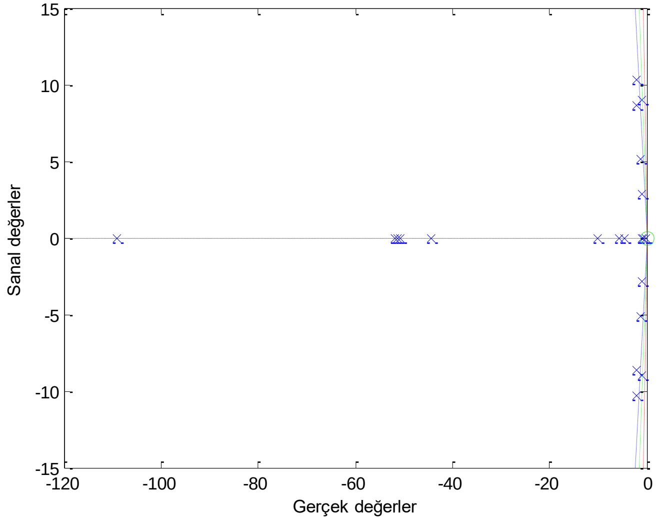

Tablo 1 SVC-POD, TY 2 model kullanıldığında küçük sinyal kararlılığı sonuçları

Sıra	**Özdeğerler (λ)**	**Frekans**	**Baskın değerler**	**Çalışma Modları**
13,14	-0.97883±j8.9687	1.4359	Delta1, Omega 1	Yerel Alan
21,22	1.0842±j2.87	0.48828	Delta2, TY 2	Bölgeler arası alan

Şekil 4 SVC-POD, TY 2 model ve yakıt hücresi kullanıldığında elde edilen sonuçlar

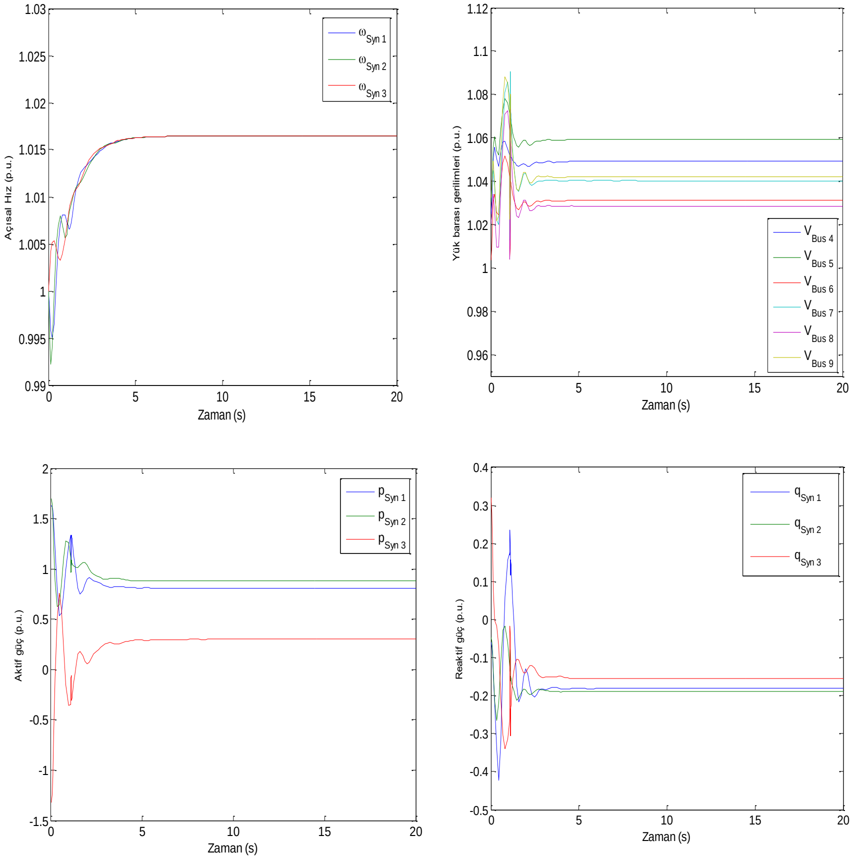

Şekil 5 SVC-POD, TY 2 model kullanımı ile gerçek-sanal değerler

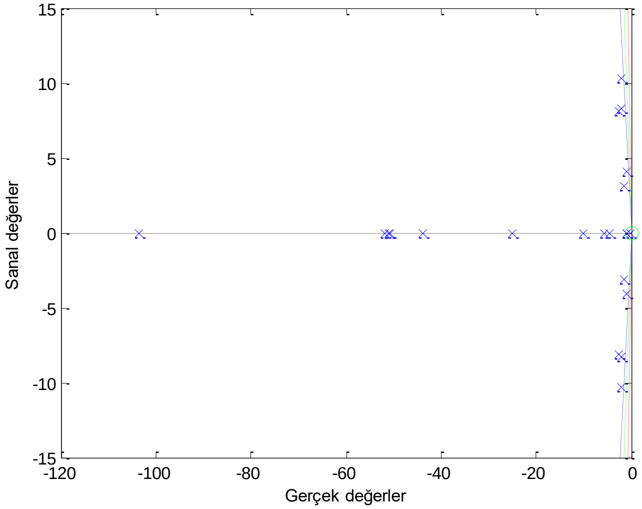

Tablo 2 SVC-POD, TY 2 model ve yakıt hücresi kullanıldığında küçük sinyal kararlılığı sonuçları

Sıra	**Özdeğerler (λ)**	**Frekans**	**Baskın değerler**	**Çalışma Modları**
17,18	-0.88258±4.0909	0.66607	Delta3, Omega3	Bölgeler arası alan
19,20	-1.4953 ±j3.1113	0.5494	Delta2, Delta 1	Bölgeler arası alan

Şekil 4 ve Şekil 5'te elde edilen sonuçlar detaylı olarak incelendiğinde SVC-POD ve TY 2 modelin kullanılması ile senkron generatör açısal hız, yük barası gerilimleri, senkron generatör aktif ile reaktif güçlerin kısa süre içerisinde kararlı hale geldikleri görülmüştür. Bunun yanı sıra geçici durum esnasında oluşan salınımların da kısa süre içerisinde sönümlendiği gözlemlenmiştir. Ancak bazı senkron generatör parametreleri ve yük baralarında salınımların daha uzun sürede kararlı hale geldiği ve salınımların azaldığı görülmüştür. SVC-POD, TY 2 model kullanıldığında gerçek-sanal değer sonuçları irdelendiğinde, 28 tane katılım faktörü değeri hesaplanmıştır. Bunların 27 tanesinin negatif olduğu, 1 tanesinin sıfır olduğu gözlemlenmiştir. Bunun yanı sıra 5 tane de karmaşık kutup olduğu görülmüştür. SVC-POD, TY 2 model kullanıldığında küçük sinyal kararlılığı analizinde sıra 13-14'te sistemin kararlı olduğu, sıra 21-22'de sistemin kararsız olduğu görülmektedir. Sıra 13-14'te baskın parametreler senkron generatör 1 açı ve açısal hızı olurken, sıra 21-22'de senkron generatör 2 açı ve TY modelin olduğu görülmüştür. Sıra 13-14'te frekans değeri 1.4359 olurken, sıra 21-22'de frekans değeri 0.48828 olmuştur. Çalışma modlarında sıra 13-14'te yerel alan olurken, sıra 21-22'de bölgeler arası alan olmuştur.

SVC-POD, TY 2 model ve yakıt hücresinin kullanılması ile elde edilen sonuçlar Şekil 6 ve Şekil 7'de gösterilmiştir. Senkron generatör açısal hız, yük barası gerilimleri, senkron generatör aktif ile reaktif güçlerinin bu kullanılan modeller sayesinde kısa süre içerisinde kararlı hale geldikleri tespit edilmiştir. Bu modeller sayesinde geçici durum esnasında oluşan salınımların da hızlıca sönümlendiği görülmüştür. SVC-POD, TY 2 model ve yakıt hücresi kullanıldığında gerçek-sanal değer sonuçları irdelendiğinde, 28 tane katılım faktörü değeri hesaplanmıştır. Bunların 27 tanesinin negatif olduğu, 1 tanesinin sıfır olduğu gözlemlenmiştir. Bunun yanı sıra 5 tane de karmaşık kutup olduğu görülmüştür. SVC-POD, TY 2 model ve yakıt hücresi kullanıldığında küçük sinyal kararlılığı analizinde sıra 17-18'de ve sıra 19-20'de sistemin kararlı olduğu görülmektedir. Sıra 17-18'de baskın parametreler senkron generatör 3 açı ve açısal hızı olurken, sıra 19-20'de senkron generatör 2 açı ve senkron generatör 1 açı olduğu görülmüştür. Sıra 17-18'de frekans değeri 0.66607 olurken, sıra 19-20'de frekans değeri 0.5494 olmuştur. Çalışma modlarının her ikisinde de bölgeler arası alan olmuştur.

Sonuçlar

Yapılan bu çalışmada SVC-POD'un kullanımının geçici olaylar durumlarında kararlılık ve salınımlar açısından daha etkili olması için senkron generatörde kullanılan TY model ve çok baralı sistemde baraya bağlanan yakıt hücresi ile geliştirilmesi amaçlanmıştır. Senkron generatör parametreleri ve bara gerilimlerinin geçici durum cevapları, gerçek-sanal değerler ve küçük sinyal kararlılığı analizleri detaylı olarak karşılaştırılmıştır. SVC-POD, TY 2 model ile SVC-POD, TY 2 model ve yakıt hücresinin kullanılması ile yapılan karşılaştırmalarda yakıt hücresinin sistem üzerinde etkili olduğu hem geçici kararlılık hem de küçük sinyal kararlılığında doğrulanmıştır. Karşılaştırmalarda, gerçek-sanal değerlerin benzer sonuçlar verdiği görülmüştür. Özellikle de senkron generatör açısının baskın parametrelerde etkili olduğu bu çalışmada görülmüştür. Yapılan bu çalışma ile SVC-POD, TY 2 model ve yakıt hücresinin kullanımının, diğer FACTS cihazları ile çeşitli analizler yapılabilmesine ve senkron generatörde kullanılan otomatik gerilim regülatörleri ve güç sistemi kararlı kılıcısı modelleri ile kullanılabilmesine zemin hazırlamaktadır.

Kaynakça

Abido, M. A., & Abdel-Magid, Y. L. (2003a). Coordinated design of a PSS and an SVC-based controller to enhance power system stability. ,. *International journal of electrical power & energy systems, 25*(9), 695-704.

Abido, M. A., & Abdel-Magid, Y. L. (2003b). Power system stability enhancement via coordinated design of a PSS and an SVC-based controller. . *In 10th IEEE International Conference on Electronics, Circuits and Systems, ICECS 2003. Proceedings of the 2003. 2*, s. 850-853. Sharjah, United Arab Emirates: IEEE.

Ayres, H. M. (2010a). A didactic procedure for designing power oscillation dampers of FACTS devices, . *Simulation Modelling Practice and Theory, 18(6), 896-909*, 896-909.

Ayres, H. M., Kopcak, I., Castro, M. S., Milano, F., & Costa, F. V. (2010). A didactic procedure for designing power oscillation dampers of FACTS devices,. *Simulation Modelling Practice and Theory, 18*(6), 896-909.

Bhole, S. S., & Nigam, P. (2015). Improvement of voltage stability in power system by using SVC and STATCOM. *International Journal of Advanced Research in Electrical, Electronics and Instrumentation Engineering, 4* (2), 76-81.

Ćalasan, M., Konjić, T., Kecojević, K., & Nikitović, L. (2020). Optimal allocation of static var compensators in electric power systems. . *Energies, 13*(12), 3219-3243.

Castro, M. S., Ayres, M. S., Da Costa, V. F., & Da Silva, L. C. (2007). Impacts of the SSSC control modes on small-signal and transient stability of a power system,. *Electric Power Systems Research,, 77*(1), 1-9.

Dehgani, A., Hakimzadeh, M., Habibi, A., & Afroozi, N. M. (2014). Small Signal Stability Enhancement for Hybrid Power Systems By SVC. World Academy of Science, Engineering and Technology. *International Journal of Electrical, Computer, Energetic, Electronic and Communication Engineering*, 1623-1627.

Ding, R., Meng, C., & Qiao, Y. (2015). (2015, June). The coordinating control of voltage and reactive power between SVC and DFIG after LVRT. *In 2015 IEEE Eindhoven PowerTech* (s. 1-5). Eindhoven, Netherlands: IEEE.

Essallah, S., Bouallegue, A., & Khedher, A. (2019). Integration of automatic voltage regulator and power system stabilizer: small-signal stability in DFIG-based wind farms. *Journal of Modern Power Systems and Clean Energy, 7*(5), 1115-1128.

Farsangi, M. M., Nezamabadi-Pour, H., Song, Y. H., & Lee, K. Y. (2007). Placement of SVCs and selection of stabilizing signals in power systems. . *IEEE Transactions on Power Systems,, 22*(3), 1061-1071.

Kamarposhti, M. A., & Alinezhad, M. (2009). Comparison of SVC and STATCOM in static voltage stability margin enhancement. *International Journal of Electrical and Computer Engineering, 2*, 297-302.

Karpagam, N., Devaraj, D., & Subbaraj, P. (2010). Improved fuzzy logic controller for SVC in power system damping using global signals. *Electrical engineering, 91* , 395-404.

Khan, S., Meena, R., & Bhowmick, S. (2015). Small signal stability improvement of a single machine infinite bus system using SVC. *In 2015 Annual IEEE India Conference (INDICON)* (s. 1-5). New Delhi, India: IEEE.

Liu, H., Xu, Z., & Gao, Z. (2001). Study on SSR characteristics of power systems with static VAr compensator. *In Seventh International Conference on AC-DC Power Transmission* (s. 193-198). London, UK: IET.

Milano F. (2005). An open source power system analysis toolbox. *IEEE Transactions on Power systems,, 20*(3), 1199-1206.

Milano, F. (2015). Small-signal stability analysis of large power systems with inclusion of multiple delays. *IEEE Transactions on Power Systems*, 3257-3266.

Mohammadpour, H. A., & Santi, E. (2022). Modeling of DFIG-based Wind farm for SSR Analysis. P. S. Diniz içinde, *In Analysis of Sub-synchronous Resonance (SSR) in Doubly-fed Induction Generator (DFIG)-Based Wind Farms Synthesis Lectures on Power Electronics* (s. 5-24). Cham: Springer Interantional Publishing.

Rahim, A. H., Nowicki, E. P., & Malik, O. P. (2006). Enhancement of power system dynamic performance through an on-line self-tuning adaptive SVC controller. . *Electric Power Systems Research, 76*(9), 801-807.

Rezaie, H., & Kazemi-Rahbar, M. H. (2019). Enhancing voltage stability and LVRT capability of a wind-integrated power system using a fuzzy-based SVC. *Engineering Science and Technology, an International Journal, 22*(3), 827-839.

Sabai, N., Maung, H. N., & Win, T. (2008). Voltage control and dynamic performance of power transmission system using static var compensator. *World Academy of Science, Engineering and Technology, 42*, 426.

Shaaban, S. M., & Mesalam, Y. I. (2022). SVC parameters optimization using a novel integrated MCDM approach. *Symmetry, 14*(4), 702-726.

Sode-Yome, A., & Mithulananthan, N. (2004). Comparison of shunt capacitor, SVC and STATCOM in static voltage stability margin enhancement. *International Journal of Electrical Engineering Education, 41*(2), 158-171.

Sujatha, S., Anita, R., Selvan, P., & Selvakumar, S. (2015). Impact of static VAR compensator in stability and harmonics mitigation for real time system with cogeneration. . *Indian Journal of Science and Technology, 8*(12), 1-11.

Thukaram, D., Khincha, H. P., & Ravikumar, B. (2004). Harmonic minimization in the operation of static VAR compensators for unbalanced reactive power compensation.. (Vol. 1, pp. 328. *In 2004 International Conference on Power System Technology, PowerCon 2004. 1*, s. 328-334. Singapore: IEEE.

Uong, S., & Ngamroo, I. (2015). Coordinated control of DFIG wind turbine and SVC for robust power system stabilization. *In 2015 12th International Conference on Electrical Engineering/Electronics, Computer, Telecommunications and Information Technology (ECTI-CON)* (s. 1-6). Hua Hin, Thailand: IEEE.

Wang, Y. P., Hur, D. R., Chung, H. H., Watson, N. R., Arrillaga, J., & Matair, S. S. (2000). A genetic algorithms approach to design an optimal PI controller for static VAr compensator. *In PowerCon 2000. 2000 International Conference on Power System Technology. Proceedings (Cat. No.00EX409)* (s. 1557-1562). Perth, WA, Australia: IEEE.

Xu, L. (2012). Coordinated control of SVC and PSS for transient stability enhancement of multi-machine power system.,. *TELKOMNIKA Indonesian Journal of Electrical Engineering, 11*(2), 1054-1062.

Yildirim, B., & Gencoglu, M. T. (2018). (2018). Oscillatory stability and eigenvalue analysis of power system with microgrid. *Electrical Engineering, 100*(4), 2351-2360.

Zhang, Z. Q., & Xiao, X. N. (2009). Analysis and mitigation of SSR based on SVC in series compensated system. *In 2009 International Conference on Energy and Environment Technology. 2*, s. 65-68. Guilin, China: EEE.

CHAPTER 2

ARTIFICIAL INTELLIGENCE AND ADVANCED DEEP LEARNING–BASED EARLY DIAGNOSIS AND INTERPRETATION/PRE-DIAGNOSIS OF PSYCHOLOGICAL DISORDERS USING ELECTROENCEPHALOGRAPHY (EEG) DATA

Ali Berkan URAL[1]*,

Muhammed Emin ÖZYILMAZ[2],

Hümeyra KARADENİZ[3]

ABSTRACT

The early identification of psychological and neuropsychiatric disorders is crucial for improving clinical outcomes and preserving patients' quality of life. Conventional diagnostic procedures largely rely on clinical interviews, subjective rating scales, and expert judgment, which may lead to delayed diagnosis and variability in interpretation. Electroencephalography (EEG), with its ability to monitor brain electrical activity at the millisecond level, has emerged as a powerful tool for revealing functional alterations underlying psychological disorders. Recent advances in artificial intelligence (AI), particularly deep learning (DL) approaches, along with improvements in computational platforms such as MATLAB, have enabled the automated analysis of EEG signals. These developments have facilitated the creation of early diagnostic and decision-support systems, thereby accelerating academic and clinical research in this field. This chapter provides a comprehensive overview of the use of EEG signals for the early detection of psychological disorders. Classical machine learning and advanced deep learning approaches, feature extraction strategies, modeling techniques, and explainable artificial intelligence concepts are discussed in detail. In addition, the strengths and limitations of current studies are examined, and future research directions are outlined.

Keywords: EEG, Brain mental problems, Artificial Intelligence, Deep Learning, MATLAB

---

[1] Assoc. Prof., Department of Electrical and Electronics Engineering, Circuits and Systems/Biomedical, Kafkas University, Kars, 36000, TURKEY, ORCID: 0000-0001-5176-9280

[2] Psychological Consultant, Akademi Special Training Center, Kars, 36000, TURKEY,ozylmzmuhammed@gmail.com, ORCID: 0009-0008-3441-7513

[3] B.Sc. Student, Department of Electrical Electronics Engineering, Kafkas University, Kars, Turkey, hmyr853@gmail.com, ORCID: 0009-0002-9886-7114

*Corresponding author: berkan.ural@kafkas.edu.tr; uralberkan@gmail.com

1. INTRODUCTION

Psychological disorders are widely recognized as a major public health concern due to their increasing global prevalence and their long-term impact on individuals' well-being and functionality (Nunes et al., 2019; Kaur et al., 2019; Templin&Henson, 2006). Conditions such as depression, anxiety disorders, attention deficit hyperactivity disorder (ADHD), bipolar disorder, and schizophrenia lead to significant alterations in cognitive performance, emotional regulation, and behavioral patterns (Zhou et al., 2019). The diagnosis of these disorders is predominantly based on clinical interviews and self-report assessment scales, and the absence of objective biological markers often contributes to diagnostic uncertainty and delayed intervention (Scherer et al., 2013).

Electroencephalography (EEG) is a non-invasive, cost-effective, and high–temporal resolution technique that is widely used to investigate brain function (Ahmed et al., 2024). Alterations in these oscillatory dynamics observed in psychological disorders position EEG as a promising source of potential neurophysiological biomarkers (Kopanska et al., 2022).

Adolescence represents a critical neurodevelopmental period characterized by rapid structural and functional brain changes, particularly in the prefrontal cortex, limbic system, and fronto-striatal circuits (Simkin et al., 2014). These neural systems are closely associated with emotional regulation, impulse control, and executive functions. During this stage, individuals are more vulnerable to the onset of psychiatric conditions such as depression, anxiety disorders, and attention deficit hyperactivity disorder (ADHD). Electroencephalography (EEG), due to its high temporal resolution and non-invasive nature, provides a practical and objective tool for monitoring neural activity in adolescents (Roohi-Azizi et al., 2017). Studies have demonstrated that alterations in specific EEG frequency bands, such as increased theta activity, reduced beta power, or abnormal frontal alpha asymmetry can reflect underlying emotional and cognitive dysregulation. These neurophysiological indicators may serve as early biomarkers for identifying adolescents at risk of developing mental health disorders (Levy&Kennard, 1953).

In addition, the integration of artificial intelligence and deep learning methods with EEG analysis has significantly improved the sensitivity of early detection systems in adolescent populations (Andrew et al., 2023). Machine learning algorithms can identify subtle and complex patterns in EEG signals that may not be apparent through conventional statistical analyses. For instance, convolutional neural networks and recurrent neural networks have been employed to classify depressive symptoms, anxiety-related neural responses, and attention deficits using EEG data collected during cognitive or emotional tasks (Alim&Imtiaz, 2023). These approaches enable the development of automated screening tools that can support clinicians, school counselors, and researchers in early risk assessment. Early identification through EEG-based systems may facilitate timely interventions, personalized therapy planning, and improved long-term mental health outcomes for adolescents (Malik et al., 2018).

Childhood is a formative period in which brain plasticity is at its peak, and neural circuits responsible for attention, learning, emotional processing, and social behavior are actively developing (McVoy et al., 2019). During this stage, neurodevelopmental and psychological disorders such as ADHD, autism spectrum disorders, anxiety, and early-onset mood disorders may begin to emerge. EEG is particularly suitable for pediatric populations because it is safe, non-invasive, and relatively tolerant of movement compared to other neuroimaging modalities. EEG-based studies in children have reported characteristic patterns, such as elevated theta/beta ratios in ADHD, altered connectivity in autism spectrum conditions, and abnormal alpha or gamma activity in anxiety-related states. These findings suggest that EEG can provide objective physiological markers for identifying atypical neural development at an early stage (Simkin et al., 2014).

Furthermore, EEG combined with artificial intelligence techniques offers promising opportunities for large-scale, automated screening in pediatric settings. Deep learning models can analyze multi-channel EEG data to detect developmental deviations in neural activity patterns, even before behavioral symptoms become clinically evident. This capability is especially valuable in early childhood, where subjective assessments may be limited by communication difficulties or developmental variability (Matsuura et al., 1993). By integrating EEG-based biomarkers with behavioral and cognitive assessments, clinicians can obtain a more comprehensive understanding of a child's neurodevelopmental status. Early detection through such systems can support timely educational planning, targeted interventions, and individualized therapeutic strategies, ultimately improving developmental trajectories and quality of life for affected children.

Artificial intelligence–based analytical approaches enable the automatic extraction of meaningful patterns from high-dimensional and complex EEG data. In particular, deep learning models can learn directly from raw or minimally processed EEG signals, thereby reducing the need for manual feature engineering (Jasper, 1949). These technological advances have paved the way for novel and promising approaches aimed at the early detection and objective assessment of psychological disorders.

2. EEG-BASED EARLY ASSESSMENT AND ANALYSIS OF PSYCHOLOGICAL DISORDERS

2.1 Fundamental Characteristics of EEG Signals

Electroencephalography (EEG) signals are low-amplitude biological recordings obtained through electrodes positioned on the scalp (Pascucci et al., 2025). Because of their weak amplitude and biological origin, these signals are highly susceptible to various sources of noise and artifacts, including eye blinks, muscle activity, and external electromagnetic interference. For this reason, a comprehensive preprocessing stage is essential to ensure reliable and meaningful analysis.

EEG activity is commonly categorized into several frequency bands:

- Delta (0.5–4 Hz): Associated with deep sleep and subconscious processes
- Theta (4–8 Hz): Related to emotional processing and memory functions
- Alpha (8–13 Hz): Linked to relaxed states and attentional regulation
- Beta (13–30 Hz): Reflects active thinking and cognitive engagement
- Gamma (>30 Hz): Represents higher-order cognitive integration processes

In various psychological disorders, significant alterations have been observed in the power distribution and synchronization patterns of these frequency bands, suggesting their potential as neurophysiological indicators.

2.2. EEG Findings in Psychological Disorders

Previous studies have reported several EEG-based indicators associated with different psychiatric conditions. For example, frontal alpha asymmetry has frequently been observed in individuals with depression, while increased theta/beta ratios are commonly reported in patients with attention deficit hyperactivity disorder (ADHD). In schizophrenia, disrupted functional connectivity patterns have been identified through EEG analyses. Such neural signatures may provide objective evidence to support clinical diagnosis. However, the high degree of inter-individual variability limits their reliability as standalone diagnostic criteria.

3. MATERIAL AND METHODS

3.1 Data Acquisition and Preprocessing

The effectiveness of EEG-based artificial intelligence systems is largely determined by the quality of the recorded data. During data acquisition, factors such as electrode placement, sampling frequency, and recording duration should be carefully standardized. In the preprocessing stage, techniques including band-pass filtering, independent component analysis (ICA), and normalization are commonly applied to remove noise and artifacts and to enhance signal quality (Kumar&Mittal et al., 2021).

3.2 Feature Extraction

In conventional machine learning approaches, a variety of features are derived from EEG signals. These include statistical, temporal, spectral, and time–frequency domain characteristics. Among the most frequently used features are power spectral density measures, entropy-based metrics, and functional connectivity indicators.

3.3 Machine Learning Approaches

Algorithms such as Support Vector Machines (SVM), k-Nearest Neighbors (k-NN), and Random Forests (RF) have been extensively used in EEG-based classification tasks. These methods are capable of delivering acceptable performance levels even when the available dataset is relatively limited.

3.4 Deep Learning Models

Deep learning approaches enable the automatic representation of EEG signals, particularly through architectures such as Convolutional Neural Networks (CNNs) and Recurrent Neural Networks (RNNs) (Jain et al., 2024). Converting time–frequency representations into image-like structures has been shown to enhance classification performance in many studies.

3.5 Explainable Artificial Intelligence

In clinical applications, the interpretability of model outputs is of critical importance. Therefore, techniques such as attention mechanisms and feature importance analysis are employed to identify which EEG components contribute most significantly to the decision-making process.

4. EARLY DIAGNOSIS OF DEPRESSION, ANXIETY DISORDERS, AND ADHD USING EEG DATA WİTH ARTIFICIAL INTELLIGENCE AND DEEP LEARNING: MATLAB-BASED APPROACHES

4.1 Depression

Depression is a complex mood disorder characterized by persistent and pervasive changes in emotional state, cognitive processes, and behavior. Clinically, it extends beyond temporary sadness and is marked by symptoms such as loss of interest or pleasure, reduced energy, cognitive slowing, and feelings of worthlessness. The heterogeneous nature of depression arises from the intricate interaction of biological, psychological, and environmental factors.

4.1.1 Neurobiological Basis

In depression, functional disturbances are commonly observed within emotional regulation networks involving the prefrontal cortex, limbic system, and hippocampus. Reduced activity in frontal cortical regions weakens decision-making and cognitive control processes, while heightened or dysregulated activity in limbic structures such as the amygdala contributes to the dominance of negative emotions. At the neurochemical level, imbalances in serotonin, norepinephrine, and dopamine systems form the biochemical foundation of depressive disorders.

4.1.2 Cognitive and Behavioral Characteristics

Depression is not only an emotional condition but is also associated with significant cognitive impairment. Common findings include reduced sustained attention, weakened working memory, and slower information processing speed. These deficits negatively influence decision-making and problem-solving abilities in daily life. Behaviorally, individuals often exhibit social withdrawal, reduced motivation, and psychomotor retardation.

4.1.3 Neurophysiological Findings (EEG Perspective)

EEG analyses in individuals with depression frequently focus on alterations in alpha-band activity. Frontal alpha asymmetry suggests an imbalance in functional activity between the left and right hemispheres. Additionally, increased theta-band activity and reduced functional connectivity indicate weakened integrity of emotional regulation networks. These findings support the possibility of using EEG-derived features as objective biomarkers for depression.

4.2 Anxiety Disorders

Anxiety disorders comprise a group of psychiatric conditions characterized by excessive and uncontrollable worry, fear, and tension. These disorders are associated with exaggerated threat perception and hyperactivation of stress-response systems. In severe cases, the clinical manifestations can significantly impair an individual's daily functioning (Kan et al., 2015).

4.2.1 Neurobiological Basis

Structures such as the amygdala, insula, and anterior cingulate cortex play central roles in anxiety disorders. Heightened sensitivity of the amygdala leads to the misinterpretation of environmental stimuli as threats. This process results in overactivation of the hypothalamic–pituitary–adrenal (HPA) axis, causing chronically elevated levels of stress hormones (Mohan et al., 2016).

4.2.2 Cognitive and Behavioral Characteristics

At the cognitive level, anxiety is characterized by persistent worry, negative expectations, and a tendency toward catastrophic thinking. Attention becomes overly focused on perceived threats, leading to inefficient use of cognitive resources. Behaviorally, avoidance, restlessness, and physical tension are typical features of anxiety disorders.

4.2.3 Neurophysiological Findings

EEG studies have associated anxiety disorders with increased activity in the beta and gamma frequency bands. This pattern reflects a persistent state of cortical hyperarousal. Moreover, increased synchronization within fronto-limbic networks suggests excessive activation of anxiety-related cognitive processes (Mohammadzadeh et al., 2016).

4.3 Attention Deficit Hyperactivity Disorder (ADHD)

ADHD is a neurodevelopmental disorder characterized by impaired sustained attention, impulsivity, and hyperactivity. Although symptoms typically emerge during childhood, they often persist into adolescence and adulthood. ADHD can significantly affect academic performance, occupational functioning, and social interactions.

Depression and ADHD are among the most prevalent psychiatric conditions affecting cognitive functioning, attention processes, and emotional regulation. Diagnostic procedures are largely based on behavioral observations and subjective rating scales, which can complicate early and objective assessment. EEG, with its high temporal resolution, provides a powerful tool for investigating the neurophysiological mechanisms underlying these disorders. Recent advances in artificial intelligence and deep learning have enabled the development of automated, high-accuracy early diagnostic systems based on EEG data. In this section, EEG patterns associated with depression and ADHD are examined in the context of signal processing, feature extraction, machine learning, and deep learning approaches within the MATLAB environment. Mathematical models, visualization techniques, and explainable AI perspectives are also discussed.

4.3.1 Neurobiological Basis

In ADHD, structural and functional differences have been reported in attention and executive control networks involving the prefrontal cortex, basal ganglia, and cerebellum. Dysregulation in dopaminergic and noradrenergic systems reduces the efficiency of attention and impulse control mechanisms.

4.3.2 Cognitive and Behavioral Characteristics

Individuals with ADHD often show significant deficits in sustained attention, planning, and organizational skills. Impulsivity results in difficulties filtering behavioral responses, while hyperactivity—particularly in childhood—manifests as motor restlessness. These symptoms can hinder adaptation to environmental demands.

4.3.3 Neurophysiological Findings

One of the most widely reported EEG indicators of ADHD is an elevated theta-to-beta ratio. An increase in theta-band activity is generally associated with reduced cognitive control and attentional instability, whereas decreased beta-band activity reflects deficiencies in executive functioning. This characteristic pattern has been extensively utilized as an EEG-based marker for the early identification of ADHD.

In general, although depression, anxiety disorders, and ADHD present with distinct clinical manifestations, they share a common feature: disruptions in the functional organization of brain networks. In depression, neural systems related to emotional inhibition and motivational processes are primarily affected. Anxiety disorders are associated with hyperactivation of threat perception and arousal systems. In contrast, ADHD mainly involves impairments in attention and executive control networks. These differences can be distinguished through neurophysiological measurements, particularly EEG-based analyses.

Depression, anxiety disorders, and ADHD are complex psychiatric conditions involving cognitive, emotional, and behavioral dimensions. Understanding the neurobiological foundations of these disorders is essential for early diagnosis and the development of individualized treatment strategies. Objective measurement techniques such as EEG provide valuable insights into the neural dynamics underlying these conditions and serve as a strong complement to traditional clinical assessments.

Early and accurate identification of psychiatric disorders is critical for improving both quality of life and treatment outcomes. Depression, one of the most prevalent mood disorders, is characterized by cognitive slowing, reduced attention, and diminished motivation.

Across all three disorders discussed in this section, alterations in the functional organization of brain networks are observed. EEG is one of the few techniques capable of capturing these changes at a millisecond temporal resolution. MATLAB has become a standard platform in academic research due to its advanced tools for EEG signal processing and analysis. This section aims to present a comprehensive framework for the early detection of depression, anxiety disorders, and ADHD by integrating EEG, MATLAB-based analysis, and artificial intelligence/deep learning approaches.

5.1. Neurophysiological Foundations of EEG

5.1.1 EEG Frequency Bands and Their Cognitive Significance

Table 1. EEG Frequency Bands and Associated Cognitive/Psychological Functions

Band	**Range (Hz)**	**Cognitive/Psychological Association**
Delta	0.5–4	Deep sleep, subconscious processes
Theta	4–8	Emotional processing, attentional fluctuations
Alpha	8–13	Resting state, cortical inhibition
Beta	13–30	Active thinking, attention, cognitive control

Band	**Range (Hz)**	**Cognitive/Psychological Association**
Gamma	>30	High-level cognitive integration

5.2 EEG-Based Analysis of Depression

5.2.1 Frontal Alpha Asymmetry

One of the most frequently reported EEG biomarkers in depression is frontal alpha asymmetry. The difference in alpha-band power between the left and right frontal cortices is closely associated with emotional regulation processes (Kamida et al., 2016). This asymmetry reflects an imbalance in hemispheric activity and has been widely studied as a potential neurophysiological indicator of depressive states.

Frontal Alpha Asymmetry Index (Equation 1):

$$\mathrm{FAI}=\log(\mathrm{PF}_4^{a})-\log(\mathrm{PF}_3^{a}) \tag{1}$$

Here, PF_3^{a} and PF_4^{a} denote the alpha-band power measured at the left and right frontal electrodes, respectively.

5.2.2 Time–Frequency Analysis (Using MATLAB)

In individuals with depression, increased power in the alpha and theta bands is frequently reported. In MATLAB, these alterations can be visualized using time–frequency methods such as the Short-Time Fourier Transform (STFT) or wavelet-based transforms (Equation 2).

$$X(t,f) = \int_{-\infty}^{\infty} x(t)w(\tau - t)\, e^{-j2f\tau}d\tau \tag{2}$$

6. EEG-BASED ANALYSIS OF ANXIETY DISORDERS AND ADHD

6.1 Theta/Beta Ratio

One of the most commonly used EEG indicators for anxiety disorders and attention deficit hyperactivity disorder (ADHD) is the theta-to-beta ratio (TBR)**.** In individuals with ADHD, theta activity tends to increase, whereas beta activity often shows a relative decrease (Equation 3). Moreover, task-related EEG recordings in ADHD frequently reveal insufficient activation in the beta and gamma bands. Such patterns are generally interpreted as reflecting impairments in executive functioning and reduced efficiency of cognitive control mechanisms.

Theta/Beta Ratio (Equation 3):

$$\mathrm{TBR}=\mathrm{P}_{\mathrm{Q}} / \mathrm{P}_{\mathrm{R}} \tag{3}$$

This ratio is particularly informative **in** frontal and central scalp regions.

Table 2. Comparison of theta/beta ratio between healthy controls and ADHD groups

Group	Mean TBR	Clinical Interpretation
Healthy	Low	Balanced attention
ADHD	High	Impaired sustained attention

7. FEATURE EXTRACTION IN THE MATLAB ENVIRONMENT

7.1 Time-Domain and Frequency-Domain Features

Using MATLAB, a broad set of EEG features can be extracted, including:

- Mean power
- Variance
- Band-power ratios
- Spectral entropy

Spectral Entropy (Equation 4):

$$H = -\sum_i p_i \log(p_i) \qquad (4)$$

Here, p_i denotes the normalized power spectrum (i.e., a probability-like distribution derived from spectral power).

7.2 Functional Connectivity

In both depression and ADHD, the functional organization of brain networks may differ from healthy patterns. Connectivity measures such as coherence **and** phase-locking value (PLV**)** can be computed efficiently in MATLAB to quantify inter-regional coupling and synchronization.

7.3 Machine Learning and Deep Learning Approaches

7.3.1 Classical Machine Learning

Commonly employed algorithms for classifying depression and ADHD using EEG data include:

-Support Vector Machines (SVM)

Support Vector Machines are among the most widely used supervised learning methods for classifying high-dimensional, noisy, and often nonlinearly separable biosignals such as EEG. The primary objective of SVM is to identify an optimal decision boundary (hyperplane) that maximally separates samples from different classes (Boyd&Campbell, 1998).

-Core principle of SVM in EEG analysis:

Each EEG trial or subject is typically represented as a **feature vector**, which may include:

- band-power features,
- statistical descriptors,
- connectivity metrics.

SVM learns a discriminant function that **maximizes** the margin between classes in the feature space. Because EEG data are frequently not linearly separable, kernel functions play a critical role.

7.3.1.2. Common kernel functions for EEG applications:

- Linear kernel: Often preferred when the feature dimension is high but the sample size is limited.
- Radial Basis Function (RBF): Widely used to capture complex nonlinear EEG patterns.
- Polynomial kernel: Can model feature interactions, but may increase the risk of overfitting.

7.3.1.3. Advantages of SVM for EEG:

- Strong performance on small-sample EEG datasets
- Relative robustness to noise
- Effective classification when informative features are selected

7.3.1.4. Limitations:

- Kernel and hyperparameter selection can be challenging
- Computational cost increases for large EEG datasets
- Model interpretability may be limited in clinical contexts

7.3.2. Random Forest (RF)

Random Forest is an ensemble learning method formed by aggregating the outputs of many decision trees. For complex biosignals such as EEG, RF improves generalization by learning from different feature subsets and resampled training instances (Arnold, 2013).

7.3.2.1. How RF operates in EEG classification:

- Randomly samples EEG instances using **bootstrap resampling**,
- Uses random feature subsets at each split,
- Combines tree predictions through **majority voting** (classification) or averaging (regression).

This structure helps reduce overfitting, a common issue in EEG modeling.

7.3.2.2. Role of RF beyond classification:

RF is also frequently used for:

- feature importance ranking**,**
- biomarker discovery, which is especially beneficial in depression and ADHD studies for identifying discriminative frequency-band features.

Advantages:

- Less sensitive to parameter tuning
- Performs well on noisy EEG data
- Provides interpretability via feature importance measures

Disadvantages:

- Higher computational cost for very large forests
- Does not naturally model time-series dependencies
- May capture deep nonlinear structure less effectively than CNNs

7.3.3. k-Nearest Neighbors (k-NN)

k-NN is an instance-based and intuitive method used in EEG classification. A new EEG sample is labeled according to the dominant class among its nearest neighbors in feature space (Georgiou et al., 2019).

7.3.3.1. Mechanism:

- Compute a distance measure (e.g., Euclidean, Manhattan, cosine),
- Select the nearest kk neighbors,
- Assign the class via majority voting.

7.3.3.2. Importance of selecting ***kk****:*

- Small kk → higher sensitivity to noise
- Large kk → increased class overlap and reduced discrimination

In EEG studies, the optimal kk is commonly determined via **cross-validation**.

-Advantages:

- Simple and easy to implement
- No explicit training phase
- Useful for rapid baselines on small datasets

-Disadvantages:

- Performance degrades in high-dimensional EEG feature spaces
- High test-time computational cost
- Sensitive to noise and feature scaling

7.3.4. Deep Learning Models

Convolutional Neural Networks can automatically learn informative representations from EEG time–frequency maps and multichannel spatial patterns (Gupte et al., 2023). The MATLAB Deep Learning Toolbox supports efficient development and training of such architectures.

CNNs have become one of the most prominent deep learning approaches in EEG analysis, particularly because they facilitate automatic feature learning from:

- time–frequency spectrograms (2D images)
- multichannel EEG topographic maps
- raw EEG time series (1D CNNs)

These strategies substantially reduce reliance on manual feature engineering.

7.3.4.1. Interpretation of CNN layers for EEG:

- Convolution layers: capture localized temporal–spectral patterns
- Pooling layers: reduce noise and improve generalization
- Fully connected layers: map learned representations to class labels

7.3.4.2. Key strengths:

- Hierarchical, automatic feature learning
- High accuracy on large EEG datasets
- Ability to integrate time–frequency and spatial information

7.3.4.3. Challenges and limitations:

- Requires large datasets for robust training
- Computationally demanding
- Limited clinical interpretability (hence the importance of attention and XAI methods)

Overall, the selection of an EEG classification approach depends on dataset size, feature structure, clinical objectives, and available computational resources. While SVM and RF are strong and reliable choices for smaller EEG datasets, CNN-based methods are advantageous for learning complex patterns from larger datasets. k-NN is typically used as a baseline or comparative reference model.

8. MATLAB IMPLEMENTATION

8.1. Workflow

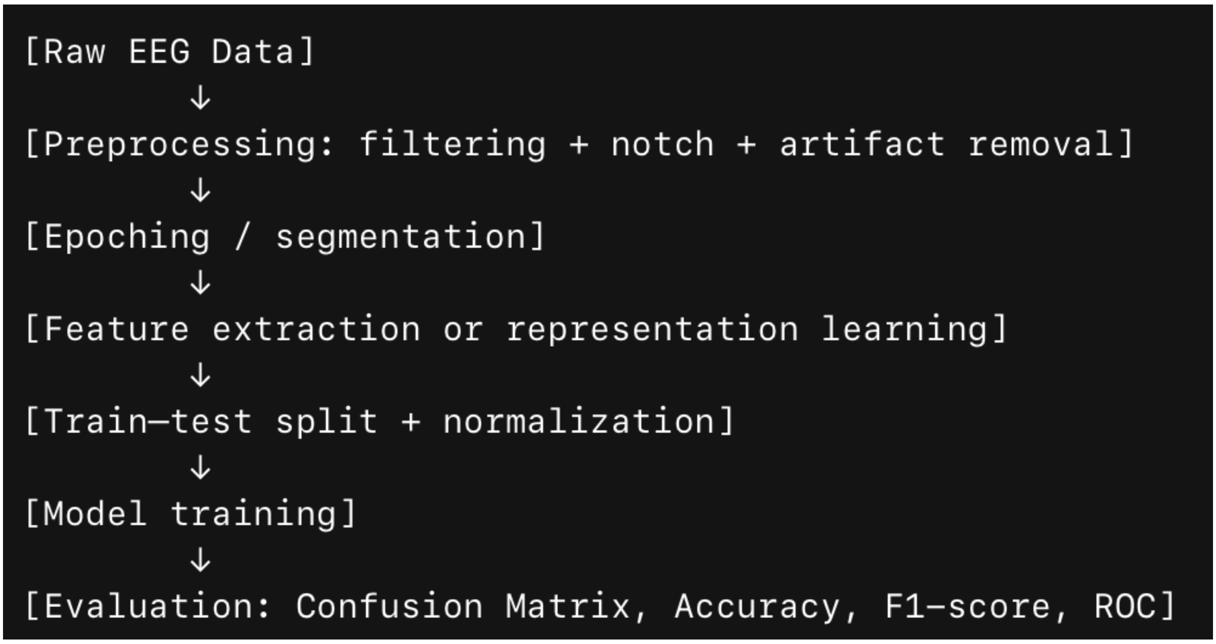

```
[Raw EEG Data]
        ↓
[Preprocessing: filtering + notch + artifact removal]
        ↓
[Epoching / segmentation]
        ↓
[Feature extraction or representation learning]
        ↓
[Train–test split + normalization]
        ↓
[Model training]
        ↓
[Evaluation: Confusion Matrix, Accuracy, F1-score, ROC]
```

8.2 General Code Workflow (Summary)

1. **Load the data** (channels × samples × epochs).
2. **Apply filtering** (band-pass and notch filters).
3. **Generate epochs** (e.g., 2-second windows with 50% overlap).
4. **Extract features** (for classical machine learning) or **generate representations** (e.g., spectrogram or time–frequency maps for CNN models).
5. **Perform train–test split** and standardize the data.
6. **Train and test the model** using the selected algorithm.
7. **Report evaluation metrics**, such as accuracy, F1-score, confusion matrix, and ROC curves.

8.3 General Codes of MATLAB

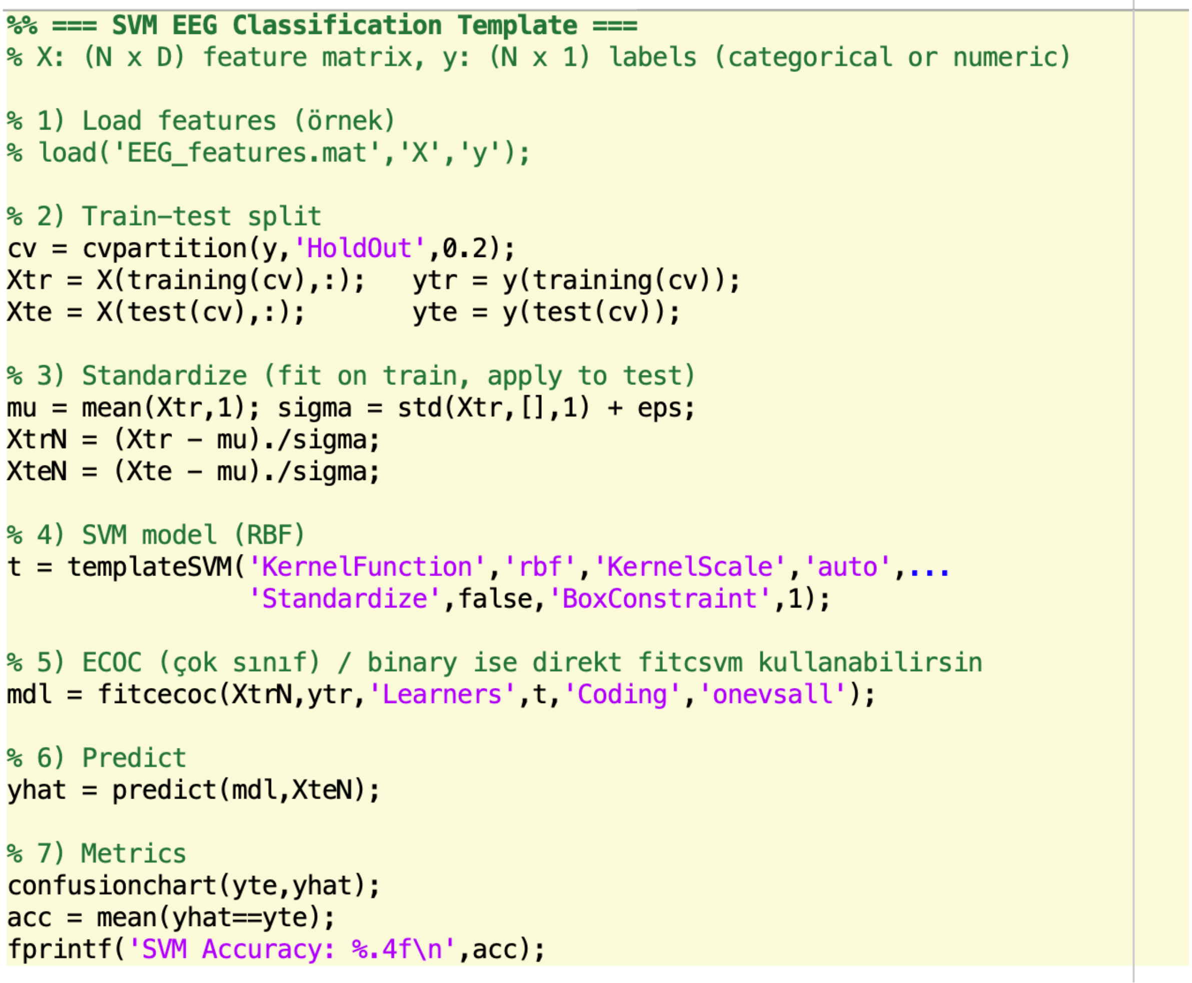

```
%% === SVM EEG Classification Template ===
% X: (N x D) feature matrix, y: (N x 1) labels (categorical or numeric)

% 1) Load features (örnek)
% load('EEG_features.mat','X','y');

% 2) Train-test split
cv = cvpartition(y,'HoldOut',0.2);
Xtr = X(training(cv),:);   ytr = y(training(cv));
Xte = X(test(cv),:);       yte = y(test(cv));

% 3) Standardize (fit on train, apply to test)
mu = mean(Xtr,1); sigma = std(Xtr,[],1) + eps;
XtrN = (Xtr - mu)./sigma;
XteN = (Xte - mu)./sigma;

% 4) SVM model (RBF)
t = templateSVM('KernelFunction','rbf','KernelScale','auto',...
                'Standardize',false,'BoxConstraint',1);

% 5) ECOC (çok sınıf) / binary ise direkt fitcsvm kullanabilirsin
mdl = fitcecoc(XtrN,ytr,'Learners',t,'Coding','onevsall');

% 6) Predict
yhat = predict(mdl,XteN);

% 7) Metrics
confusionchart(yte,yhat);
acc = mean(yhat==yte);
fprintf('SVM Accuracy: %.4f\n',acc);
```

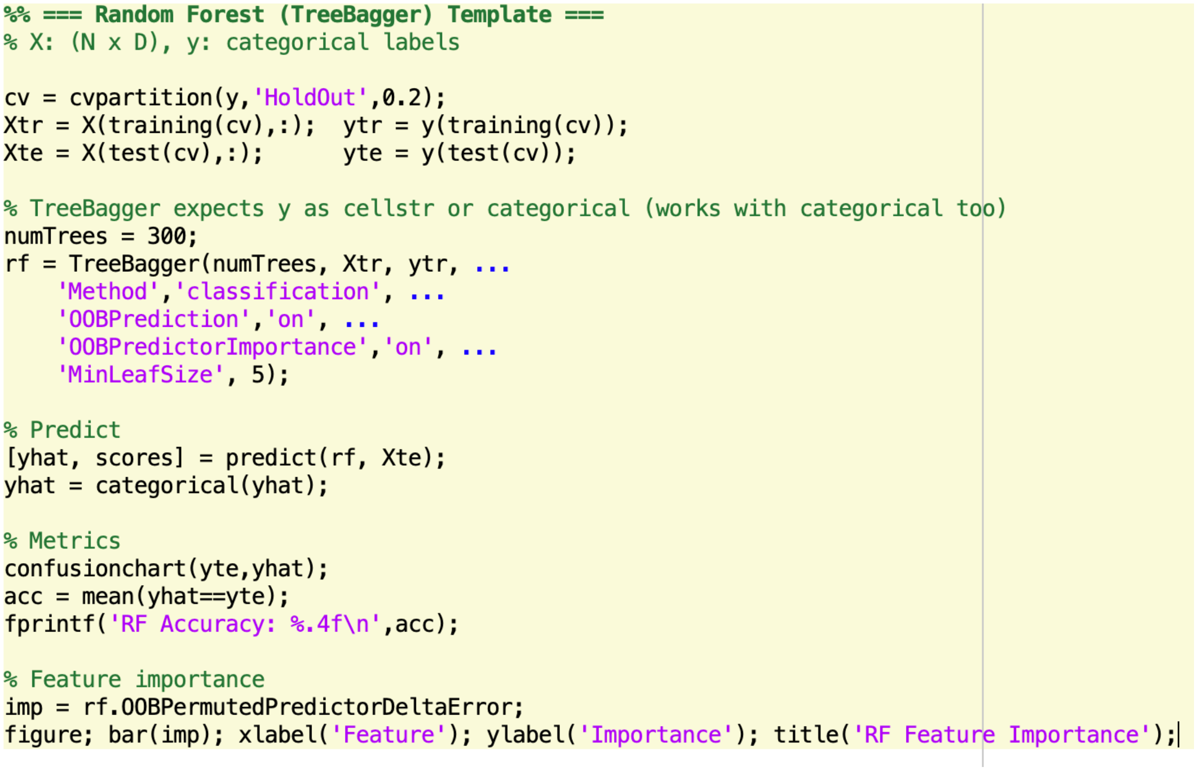

```
%% === Random Forest (TreeBagger) Template ===
% X: (N x D), y: categorical labels

cv = cvpartition(y,'HoldOut',0.2);
Xtr = X(training(cv),:);  ytr = y(training(cv));
Xte = X(test(cv),:);      yte = y(test(cv));

% TreeBagger expects y as cellstr or categorical (works with categorical too)
numTrees = 300;
rf = TreeBagger(numTrees, Xtr, ytr, ...
    'Method','classification', ...
    'OOBPrediction','on', ...
    'OOBPredictorImportance','on', ...
    'MinLeafSize', 5);

% Predict
[yhat, scores] = predict(rf, Xte);
yhat = categorical(yhat);

% Metrics
confusionchart(yte,yhat);
acc = mean(yhat==yte);
fprintf('RF Accuracy: %.4f\n',acc);

% Feature importance
imp = rf.OOBPermutedPredictorDeltaError;
figure; bar(imp); xlabel('Feature'); ylabel('Importance'); title('RF Feature Importance');
```

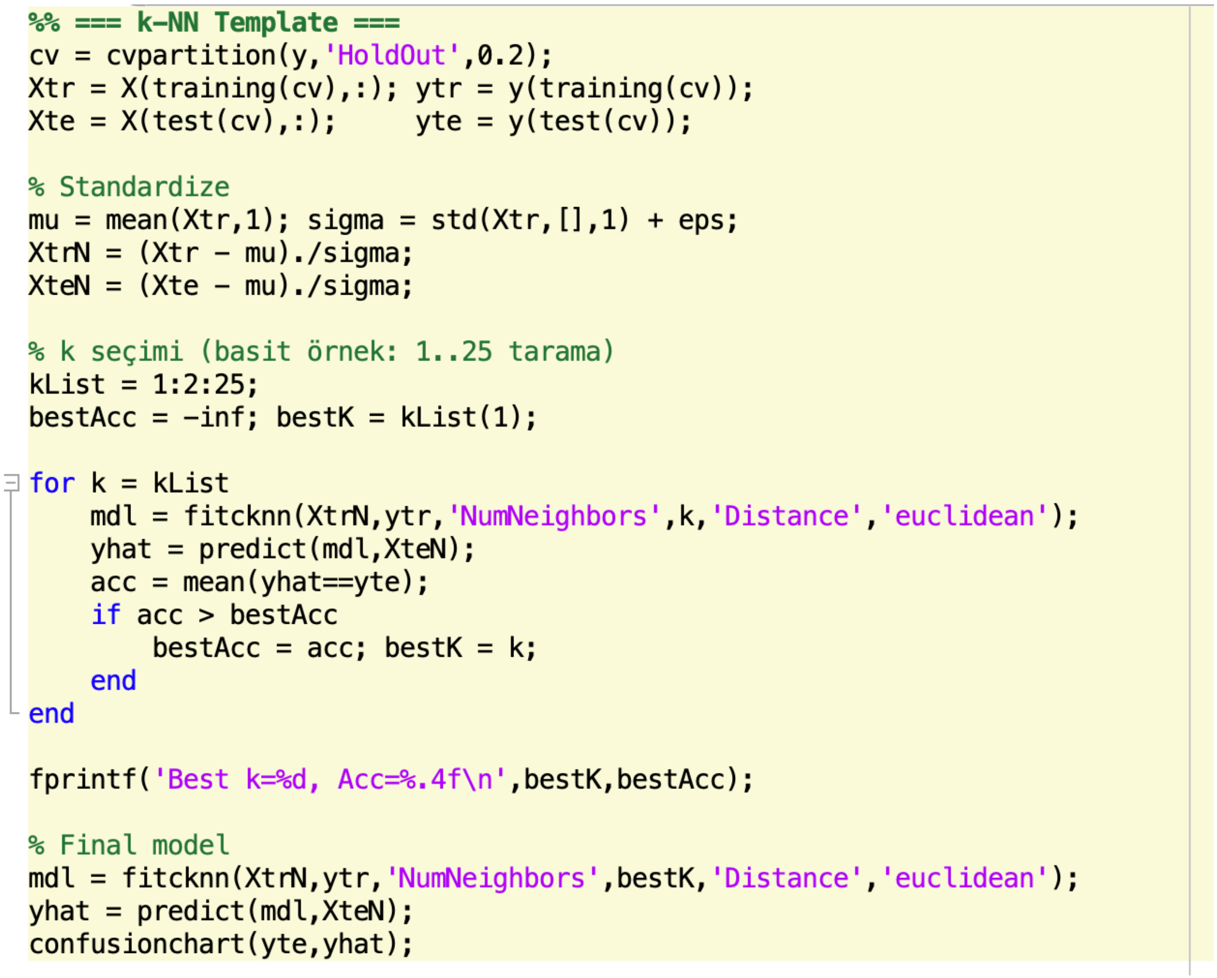

```
%% === k-NN Template ===
cv = cvpartition(y,'HoldOut',0.2);
Xtr = X(training(cv),:); ytr = y(training(cv));
Xte = X(test(cv),:);     yte = y(test(cv));

% Standardize
mu = mean(Xtr,1); sigma = std(Xtr,[],1) + eps;
XtrN = (Xtr - mu)./sigma;
XteN = (Xte - mu)./sigma;

% k seçimi (basit örnek: 1..25 tarama)
kList = 1:2:25;
bestAcc = -inf; bestK = kList(1);

for k = kList
    mdl = fitcknn(XtrN,ytr,'NumNeighbors',k,'Distance','euclidean');
    yhat = predict(mdl,XteN);
    acc = mean(yhat==yte);
    if acc > bestAcc
        bestAcc = acc; bestK = k;
    end
end

fprintf('Best k=%d, Acc=%.4f\n',bestK,bestAcc);

% Final model
mdl = fitcknn(XtrN,ytr,'NumNeighbors',bestK,'Distance','euclidean');
yhat = predict(mdl,XteN);
confusionchart(yte,yhat);
```

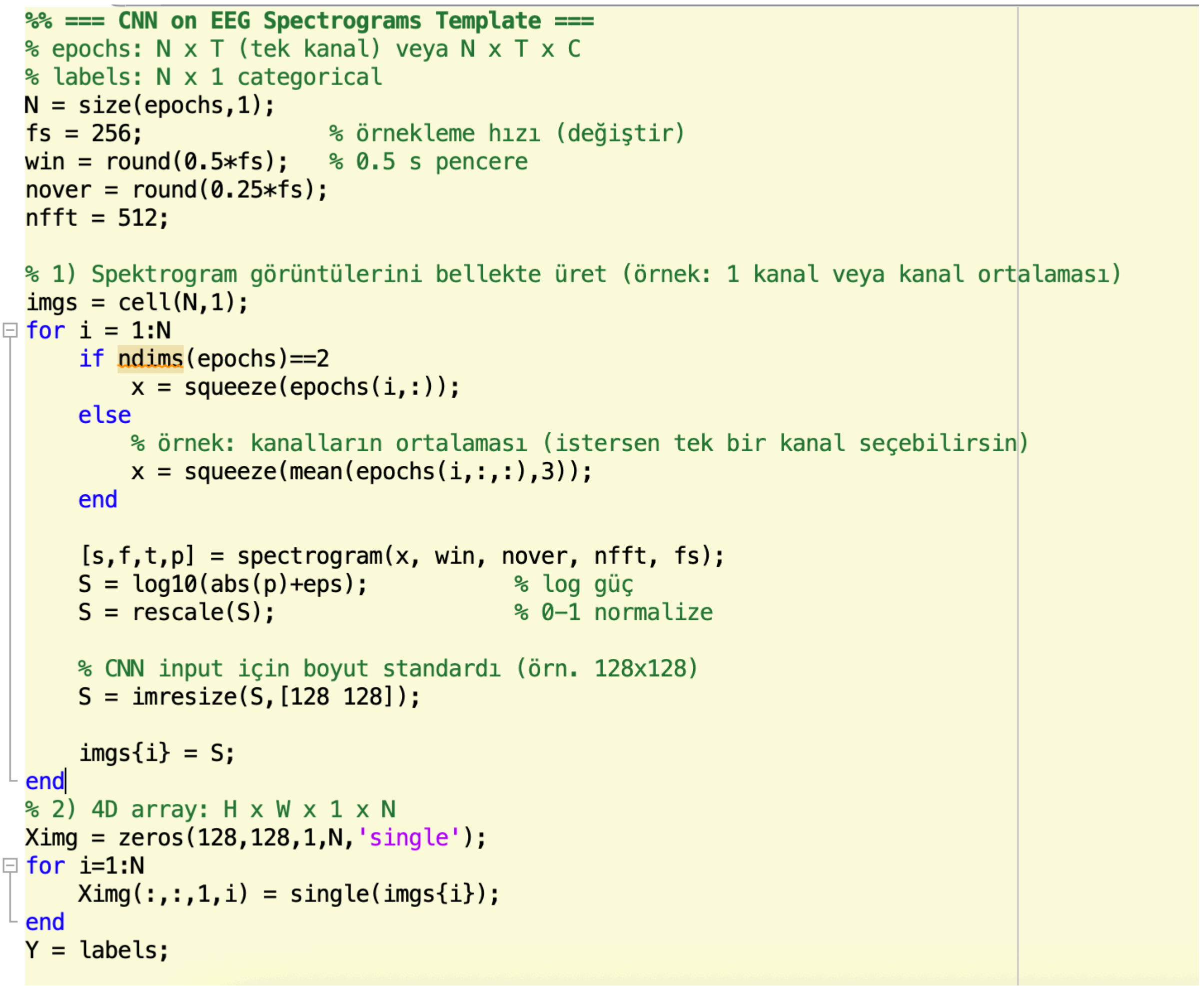

```
%% === CNN on EEG Spectrograms Template ===
% epochs: N x T (tek kanal) veya N x T x C
% labels: N x 1 categorical
N = size(epochs,1);
fs = 256;              % örnekleme hızı (değiştir)
win = round(0.5*fs);   % 0.5 s pencere
nover = round(0.25*fs);
nfft = 512;

% 1) Spektrogram görüntülerini bellekte üret (örnek: 1 kanal veya kanal ortalaması)
imgs = cell(N,1);
for i = 1:N
    if ndims(epochs)==2
        x = squeeze(epochs(i,:));
    else
        % örnek: kanalların ortalaması (istersen tek bir kanal seçebilirsin)
        x = squeeze(mean(epochs(i,:,:),3));
    end

    [s,f,t,p] = spectrogram(x, win, nover, nfft, fs);
    S = log10(abs(p)+eps);          % log güç
    S = rescale(S);                 % 0-1 normalize

    % CNN input için boyut standardı (örn. 128x128)
    S = imresize(S,[128 128]);

    imgs{i} = S;
end
% 2) 4D array: H x W x 1 x N
Ximg = zeros(128,128,1,N,'single');
for i=1:N
    Ximg(:,:,1,i) = single(imgs{i});
end
Y = labels;
```

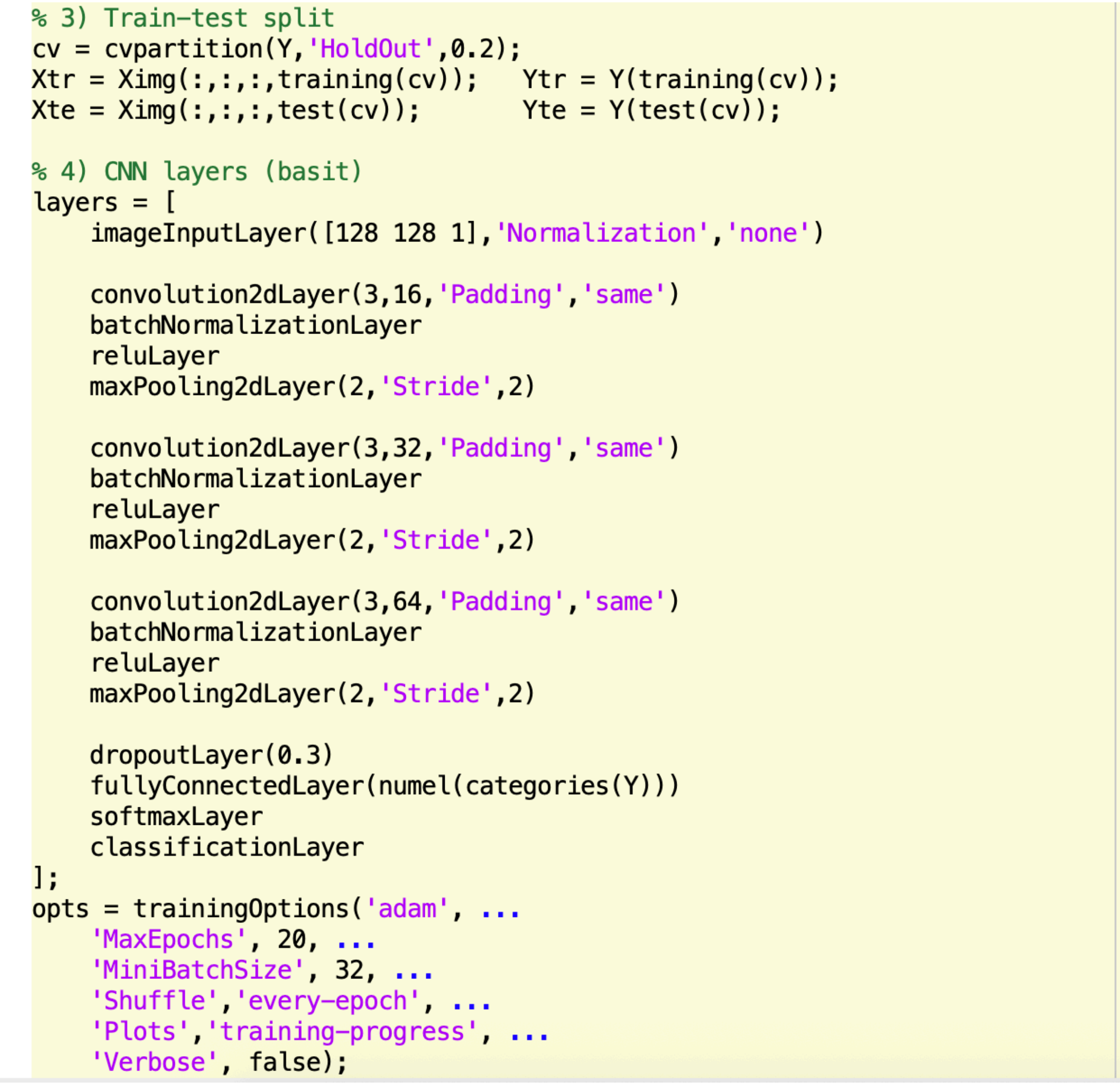

```
% 3) Train-test split
cv = cvpartition(Y,'HoldOut',0.2);
Xtr = Ximg(:,:,:,training(cv));   Ytr = Y(training(cv));
Xte = Ximg(:,:,:,test(cv));       Yte = Y(test(cv));

% 4) CNN layers (basit)
layers = [
    imageInputLayer([128 128 1],'Normalization','none')

    convolution2dLayer(3,16,'Padding','same')
    batchNormalizationLayer
    reluLayer
    maxPooling2dLayer(2,'Stride',2)

    convolution2dLayer(3,32,'Padding','same')
    batchNormalizationLayer
    reluLayer
    maxPooling2dLayer(2,'Stride',2)

    convolution2dLayer(3,64,'Padding','same')
    batchNormalizationLayer
    reluLayer
    maxPooling2dLayer(2,'Stride',2)

    dropoutLayer(0.3)
    fullyConnectedLayer(numel(categories(Y)))
    softmaxLayer
    classificationLayer
];
opts = trainingOptions('adam', ...
    'MaxEpochs', 20, ...
    'MiniBatchSize', 32, ...
    'Shuffle','every-epoch', ...
    'Plots','training-progress', ...
    'Verbose', false);
```

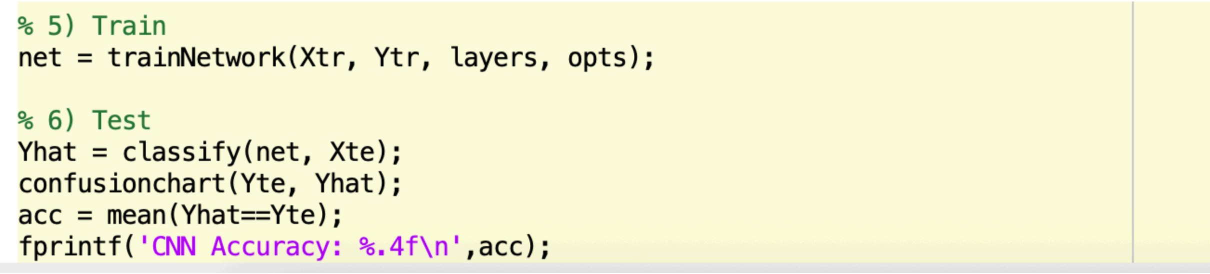

```
% 5) Train
net = trainNetwork(Xtr, Ytr, layers, opts);

% 6) Test
Yhat = classify(net, Xte);
confusionchart(Yte, Yhat);
acc = mean(Yhat==Yte);
fprintf('CNN Accuracy: %.4f\n',acc);
```

9.CONCLUSION

In this study, artificial intelligence and deep learning–based approaches for the early identification of common psychiatric conditions, such as depression, anxiety disorders, and attention deficit hyperactivity disorder (ADHD) using electroencephalography (EEG) signals have been comprehensively examined. The high temporal resolution of EEG and its ability to directly reflect neuronal activity provide a valuable opportunity to objectively investigate the neurophysiological mechanisms underlying these disorders. Signal processing, feature extraction, and classification procedures implemented within the MATLAB environment offer a powerful, flexible, and reproducible framework for both academic and clinical research.

Findings related to depression indicate that EEG patterns such as frontal alpha asymmetry, increased theta-band activity, and reduced functional connectivity may serve as distinguishing neurophysiological biomarkers of the disorder. In anxiety disorders, elevated beta and gamma activity suggests a persistent state of cortical hyperarousal, which is closely linked to heightened threat perception and excessive worry. In ADHD, an increased theta/beta ratio provides neurophysiological evidence of impairments in sustained attention and executive control mechanisms. Collectively, these findings demonstrate that each disorder exhibits both shared and disorder-specific EEG characteristics.

From a machine learning perspective, Support Vector Machines and Random Forest algorithms have been shown to achieve strong classification performance, particularly in EEG datasets with limited sample sizes. The feature importance measures provided by Random Forest models offer a notable advantage in terms of clinical interpretability. Although the k-Nearest Neighbors algorithm provides a simple and intuitive baseline for comparative studies, its performance may be limited in high-dimensional EEG feature spaces. In contrast, Convolutional Neural Networks enable automatic and hierarchical feature learning from time–frequency representations and multichannel EEG data, allowing more complex patterns to be captured.

Deep learning–based approaches represent a significant paradigm shift in EEG analysis by reducing dependence on manual feature extraction. However, their high data requirements, computational demands, and limited interpretability remain important considerations when integrating these models into clinical practice. In this context, the development of explainable artificial intelligence (XAI) techniques and hybrid modeling approaches is expected to enhance the reliability and clinical acceptance of EEG-based diagnostic support systems.

Overall, the integration of EEG data with artificial intelligence and deep learning methods demonstrates strong potential for the objective and early detection of psychiatric disorders. MATLAB-based end-to-end analysis pipelines provide researchers and clinicians with a standardized, extensible, and reproducible working environment. In the future, larger and multicenter EEG datasets will better capture inter-individual variability, while the integration of multimodal data, such as EEG signals, clinical scales, and behavioral measurements will further improve diagnostic accuracy.

In conclusion, the methods and findings presented in this study suggest that EEG-based artificial intelligence systems can play a complementary, and in some cases guiding, role in the diagnosis and monitoring of psychiatric disorders alongside traditional clinical assessments.

Further research in this field is expected to contribute significantly to the development of personalized psychiatric evaluation and treatment strategies.

REFERENCES

Ahmed, Z., Wali, A., Shahid, S., Zikria, S., Rasheed, J., & Asuroglu, T. (2024). Psychiatric disorders from EEG signals through deep learning models. IBRO Neuroscience Reports, 17, 300–310.

Alim, A., & Imtiaz, M. H. (2023). Automatic identification of children with ADHD from EEG brain waves. Signals, 4(1), 193–205.

Andrew, J., Rudra, M., Eunice, J., & Belfin, R. V. (2023). Artificial intelligence in adolescents mental health disorder diagnosis, prognosis, and treatment. Frontiers in Public Health, 11, 1110088.

Arnold, L. E. (2013). Introduction: EEG brain waves: a wave of the future or past?. Journal of Attention Disorders, 17(5), 371–373.

Boyd, W. D., & Campbell, S. E. (1998). EEG biofeedback in the schools: The use of EEG biofeedback to treat ADHD in a school setting. Journal of Neurotherapy, 2(4), 65–71.

Georgiou, E., Thanos, G. K., Kanellos, T., Doulgerakis, A., & Thomopoulos, S. C. (2019, May). Evaluating the relation between the EEG brainwaves and attention measures, and the children’s performance in REEFOCUS game designed for ADHD symptoms improvement. In Smart Biomedical and Physiological Sensor Technology XVI (Vol. 11020, pp. 189–198). SPIE.

Gupte, N., Patel, M., Pen, T., & Kurhade, S. (2023, April). Early detection of ADHD and dyslexia from EEG signals. In 2023 IEEE 8th International Conference for Convergence in Technology (I2CT) (pp. 1–5). IEEE.

Jain, A., Raja, R., Srivastava, S., Sharma, P. C., Gangrade, J., & R, M. (2024). Analysis of EEG signals and data acquisition methods: a review. Computer Methods in Biomechanics and Biomedical Engineering: Imaging & Visualization, 12(1), 2304574.

Jasper, H. H. (1949). Electroencephalography in child neurology and psychiatry. Pediatrics, 3(6), 783–800.

Kamida, A., Shimabayashi, K., Oguri, M., Takamori, T., Ueda, N., Koyanagi, Y., & Maegaki, Y. (2016). EEG power spectrum analysis in children with ADHD. Yonago Acta Medica, 59(2), 169.

Kan, D. P. X., & Lee, P. F. (2015, May). Decrease alpha waves in depression: An electroencephalogram (EEG) study. In 2015 International Conference on BioSignal Analysis, Processing and Systems (ICBAPS) (pp. 156–161). IEEE.

Kaur, P., & Sharma, M. (2019). Diagnosis of human psychological disorders using supervised learning and nature-inspired computing techniques: a meta-analysis. Journal of Medical Systems, 43(7), 204.

Kopańska, M., Ochojska, D., Dejnowicz-Velitchkov, A., & Banaś-Ząbczyk, A. (2022). Quantitative electroencephalography (QEEG) as an innovative diagnostic tool in mental disorders. International Journal of Environmental Research and Public Health, 19(4), 2465.

Kumar, J. M., & Mittal, V. K. (2021, May). EEG data acquisition system and analysis of EEG signals. In 2021 2nd International Conference for Emerging Technology (INCET) (pp. 1–5). IEEE.

Levy, S., & Kennard, M. A. (1953). The EEG pattern of patients with psychologic disorders of various ages. The Journal of Nervous and Mental Disease, 118(5), 416–428.

Malik, J., Dahiya, M., & Kumari, N. (2018). Brain wave frequency measurement in gamma wave range for accurate and early detection of depression. International Journal of Advanced Research and Innovation, 6(1), 21–24.

Matsuura, M., Okubo, Y., Toru, M., Kojima, T., He, Y., Shen, Y., & Lee, C. K. (1993). A cross-national EEG study of children with emotional and behavioral problems: a WHO collaborative study in the Western Pacific Region. Biological Psychiatry, 34(1–2), 59–65.

McVoy, M., Lytle, S., Fulchiero, E., Aebi, M. E., Adeleye, O., & Sajatovic, M. (2019). A systematic review of quantitative EEG as a possible biomarker in child psychiatric disorders. Psychiatry Research, 279, 331–344.

Mohammadzadeh, B., Sattari, K., & Lotfizadeh, M. (2016). Determining the relationship between depression and brain waves in depressed subjects using Pearson correlation and regression. Epidemiology and Health System Journal, 3(4), 376–385.

Mohan, Y., Chee, S. S., Xin, D. K. P., & Foong, L. P. (2016, December). Artificial neural network for classification of depressive and normal EEG. In 2016 IEEE EMBS Conference on Biomedical Engineering and Sciences (IECBES) (pp. 286–290). IEEE.

Nunes, L. C., Pinheiro, P. R., Pinheiro, M. C. D., Simão Filho, M., Nunes, R. E. C., & Pinheiro, P. G. C. D. (2019). Automatic detection and diagnosis of neurologic diseases. IEEE Access, 7, 29924–29941.

Pascucci, D., Menétrey, M. Q., Passarotto, E., Luo, J., Paramento, M., & Rubega, M. (2025). EEG brain waves and alpha rhythms: Past, current and future direction. Neuroscience & Biobehavioral Reviews, 106288.

Roohi-Azizi, M., Azimi, L., Heysieattalab, S., & Aamidfar, M. (2017). Changes of the brain's bioelectrical activity in cognition, consciousness, and some mental disorders. Medical Journal of the Islamic Republic of Iran, 31, 53.

Scherer, S., Stratou, G., Mahmoud, M., Boberg, J., Gratch, J., Rizzo, A., & Morency, L. P. (2013, April). Automatic behavior descriptors for psychological disorder analysis. In 2013 10th IEEE International Conference and Workshops on Automatic Face and Gesture Recognition (FG) (pp. 1–8). IEEE.

Simkin, D. R., Thatcher, R. W., & Lubar, J. (2014). Quantitative EEG and neurofeedback in children and adolescents: anxiety disorders, depressive disorders, comorbid addiction and attention-deficit/hyperactivity disorder, and brain injury. Child and Adolescent Psychiatric Clinics, 23(3), 427–464.

Templin, J. L., & Henson, R. A. (2006). Measurement of psychological disorders using cognitive diagnosis models. Psychological Methods, 11(3), 287.

Zhou, T. H., Hu, G. L., & Wang, L. (2019). Psychological disorder identifying method based on emotion perception over social networks. International Journal of Environmental Research and Public Health, 16(6), 953.

CHAPTER 3

SPIKING NEURAL NETWORKS: MODELS, COMPUTATION, AND SIMULATION TOOLS

İBRAHİM ÖZTÜRK[1]

Abstract

This chapter reviews the theoretical underpinnings and computational capabilities of Spiking Neural Networks (SNNs), the third generation of neural network models. It examines the transition from rate-based coding to temporal coding, supported by neurobiological evidence of precise inter-spike timing. A specific focus is placed on the trade-offs inherent in spiking neuron models, ranging from the biophysically rigorous Hodgkin-Huxley model to efficient abstractions like the Adaptive Exponential Integrate-and-Fire (AdEx) and the Spike Response Model (SRM). Furthermore, the chapter explores mechanisms of synaptic plasticity, such as delay selection, and evaluates current software simulation tools, benchmarking their performance across various hardware backends.

1. Introduction: The Third Generation of Neural Network Models

---

[1] Assistant Professor, Osmaniye Korkut Ata University, Department of Electrical and Electronics Engineering, Orcid: 0000-0003-3149-0527

The evolution of neural network theory is typically categorized into three distinct generations based on the computational nature of their fundamental units. The first generation relies on McCulloch-Pitts neurons, or threshold gates, which produce digital outputs. The second generation employs activation functions with continuous output values, such as sigmoid or hyperbolic tangent functions, enabling analogue computations and gradient-descent learning algorithms like backpropagation.

Spiking Neural Networks (SNNs) represent the third generation of neural network models. Unlike their predecessors, SNNs utilize the precise timing of single action potentials, or "spikes," to encode information. This paradigm shift is motivated by neurobiological evidence suggesting that traditional "firing rate" interpretations, where information is averaged over time, are insufficient to explain the speed of cortical processing. For instance, visual pattern analysis in primates occurs within timeframes (20-30 ms per processing stage) that are too short to allow for the temporal averaging required by rate-based models. Consequently, SNNs treat time as an intrinsic resource for computation, offering a model that is both biologically realistic and computationally powerful. While it is described the functional physiology (temporal coding and spike timing) that animates it, Figure 1 provides the structural skeleton (neurons and connections). Together, it is illustrated how a sparse, feed-forward architecture can achieve the biological realism and computational efficiency characteristic of the "third generation" of neural networks.

Figure 1: Schematic of a typical feed-forward SNN structure. Input layer neurons (red) are fully connected to the hidden layer (gray), which propagates signals to the output layer.

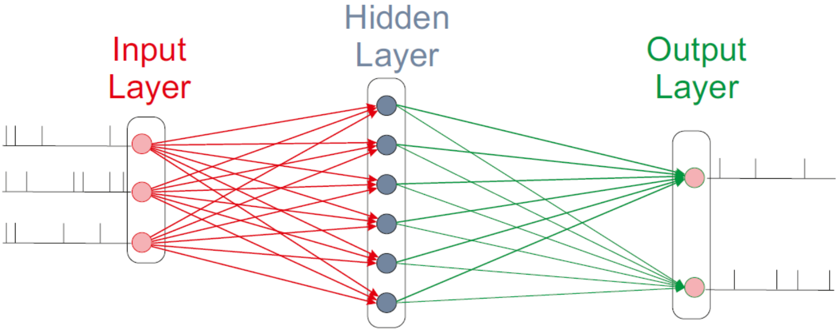

Source: From "Learning spatio-temporal spike train encodings with ReSuMe, DelReSuMe, and Reward-modulated Spike-timing Dependent Plasticity in Spiking Neural Networks," by I. Ozturk, 2017, University of York. Copyright 2017 by I. Ozturk.

2. Spiking Neuron Models: Balancing Biophysics and Efficiency

The selection of a neuron model in SNN research represents a critical trade-off between biological fidelity and computational efficiency. Models range from detailed biophysical descriptions of ionic mechanisms to phenomenological reductions that treat the neuron as a simplified circuit.

2.1. Biophysical Models: The Hodgkin–Huxley Model

Developed in 1952, the Hodgkin–Huxley (HH) model is widely considered the gold standard for describing the initiation and propagation of neuronal action potentials. As illustrated in Figure 2, the model abstracts the biological properties of the cell membrane into an equivalent electrical circuit. The lipid bilayer is represented as a capacitance (C_m), reflecting its ability to separate electrical charge. Parallel to this capacitor, the model defines specific electrical branches for ionic currents: voltage-gated sodium and potassium channels are represented as variable, nonlinear conductances ($g_{Na} and g_K$), while leak channels are modeled as a constant linear conductance (g_L). Furthermore, the electrochemical gradients that drive the flow of ions across these channels are depicted in Figure 2 as batteries (E), placed in series with each conductance.

Figure 2: The proposed equivalent electrical circuit with three channels by Hodgkin and Huxley to describe nerve excitation.

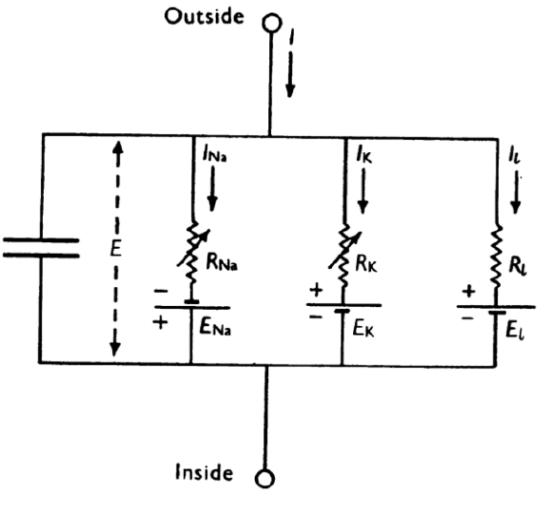

Source: Hodgkin & Huxley (1952).

While the Hodgkin-Huxley model accurately reproduces the precise shape of action potentials, refractory periods, and resting responses, the model is computationally complex and nonlinear. This capacity for detailed biophysical simulation is illustrated in Figure 3, which depicts the response of a Hodgkin-Huxley neuron to a step in external input current. As shown in the 200 ms time-course, the membrane potential (upper trace) remains stable while the input current (lower trace) is 0 nA; however, when the current increases to +0.4 nA at 160 ms, exceeding the threshold voltage, the model successfully generates a train of regular spikes. Despite this fidelity, the necessity of solving coupled nonlinear differential equations makes the model computationally prohibitive for large-scale networks. Consequently, simplified neuron models with a higher level of abstraction have been proposed to balance accuracy with efficiency. One of the most widely used models for analysing the behaviour of nerve cells is the integrate-and-fire model, developed by Louis Lapicque in 1907, which considers a neuron that emits a spike only if the total excitation is sufficiently large.

Figure 3: Simulation of a Hodgkin–Huxley neuron generating regular spikes in response to an external input current. The 200 ms time-course of the membrane potential $V_m(t)$ *(upper trace) is shown as the input current (lower trace) switches from 0 nA (subthreshold) at 20 ms to +0.4 nA (exceeding the threshold voltage) at 160 ms.*

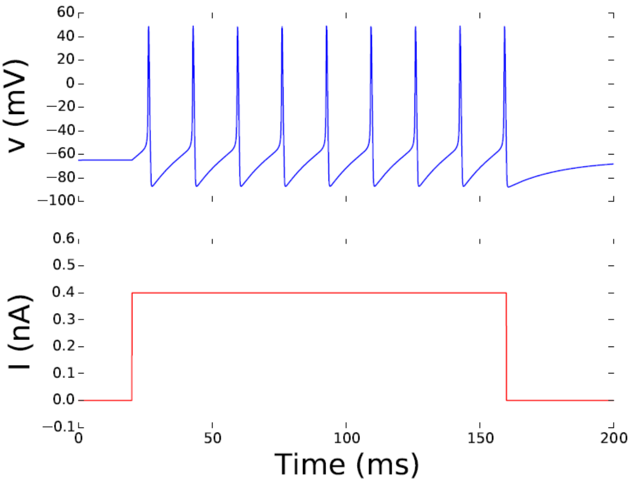

Source: From "Learning spatio-temporal spike train encodings with ReSuMe, DelReSuMe, and Reward-modulated Spike-timing Dependent Plasticity in Spiking Neural Networks," by I. Ozturk, 2017, University of York. Copyright 2017 by I. Ozturk.

The Hodgkin-Huxley model mathematically characterizes the initiation and propagation of action potentials through a system of four nonlinear ordinary differential equations that describe the conductance of ionic currents—specifically Sodium (Na^+) and Potassium (K^+)—across the cell membrane (Hodgkin & Huxley, 1952). Central to this framework is the incorporation of dimensionless gating variables (n, m, h) which evolve according to first-order kinetics to represent the voltage-dependent probabilities of ion channel activation and inactivation (Hodgkin & Huxley, 1952), Due to its inherent nonlinearity, the model captures complex dynamical behaviours, including limit cycles and Hopf bifurcations, which allows for the precise reproduction of empirical phenomena such as the specific shape of action potentials and the refractory period (Izhikevich, 2003). However, despite this high degree of biophysical fidelity, the Hodgkin-Huxley model remains computationally prohibitive for large-scale network simulations, as the requirement to solve coupled differential equations for every individual neuron imposes a significant processing overhead compared to simplified phenomenological models (Izhikevich, 2004).

2.2. Phenomenological Circuit Models

To facilitate the simulation of large networks, phenomenological models abstract biophysical details into simplified circuit behaviours.

The Leaky Integrate-and-Fire (LIF) The LIF model treats the neuron as a simple Resistor-Capacitor (RC) circuit driven by input current. The membrane potential evolves according to a linear differential equation characterized by a time constant $\tau = RC$. When reaches a specific threshold $V(t) \dots V_{th}$, a spike is recorded, and the voltage is manually reset to a value V_{reset}. While computationally efficient, the

LIF model is often criticized for being "unrealistically simple"; it lacks intrinsic adaptation variables and cannot naturally reproduce complex firing patterns like bursting without modification.

Figure 4 illustrates the response of a single Leaky Integrate-and-Fire (LIF) neuron to a step change in external input, highlighting the transition between subthreshold and suprathreshold regimes. The membrane potential (upper trace) evolves according to the dynamics of a passive RC circuit, governed by the linear differential equation, where the decay constant $\tau_m = 10\,ms$ determines the speed at which the voltage relaxes toward the steady state (Gerstner et al., 2014). Initially, at 20 ms, the input drive is insufficient to trigger a response, keeping the potential below the firing threshold. However, as the input switches to a suprathreshold level (+10 mV) at 160 ms, the membrane potential rises exponentially; upon crossing the threshold voltage, the model records a spike and instantaneously resets to a resting value (Gerstner & Kistler, 2002). Unlike biophysical models that simulate the pulse shape, this artificial reset is a modelling convention, and with the refractory period set to $t_{ref} = 0$, the neuron immediately resumes integration after every reset without a "dead time" delay (Gerstner et al., 2014).

Figure 4: Simulation of a single LIF neuron driven by an external input current. The 200 ms time-course of the membrane potential $V_{m(t)}$ *(upper trace) is shown as the current trajectory (lower trace) switches from 0 mV (subthreshold) at ms to mV (exceeding the threshold voltage* $V_{\{th\}}$*) at 160 ms. The model assumes no*

refractory period ($t_{\{ref\}} = 0$) and a decay constant of τ_m= 10 ms.

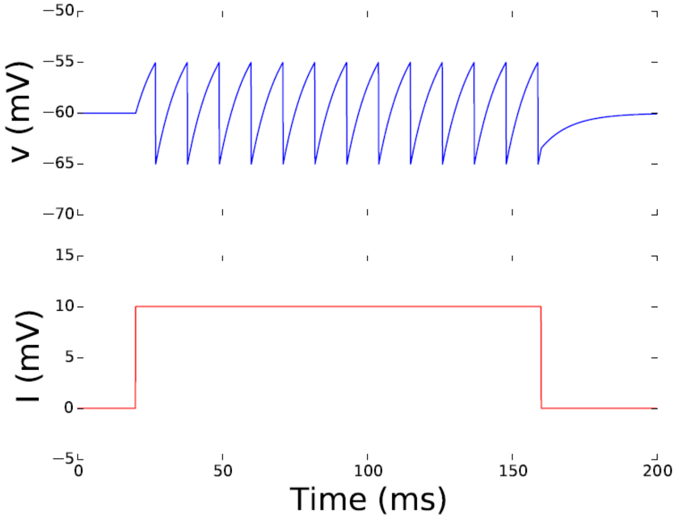

Source: From "Learning spatio-temporal spike train encodings with ReSuMe, DelReSuMe, and Reward-modulated Spike-timing Dependent Plasticity in Spiking Neural Networks," by I. Ozturk, 2017, University of York. Copyright 2017 by I. Ozturk.

The Spike Response Model (SRM) The SRM describes the membrane voltage not through differential equations, but as a linear sum of response kernels. It models the voltage as a summation of postsynaptic potentials (PSPs) caused by incoming spikes and a refractory kernel that models the neuron’s response to its own previous spikes (adaptation and refractoriness). The SRM is particularly useful for theoretical analysis of network capacity and is mathematically equivalent to Generalized Linear Models (GLM) used in statistical neuroscience.

2.3. Hybrid Models: Izhikevich and AdEx

Hybrid models aim to bridge the gap between the biological plausibility of Hodgkin–Huxley and the speed of Integrate-and-Fire.

- The Izhikevich Neuron: This model reduces biophysical dynamics to a two-dimensional system of ordinary differential equations using bifurcation theory. By tuning just four dimensionless parameters, it can reproduce the firing patterns of all known types of cortical neurons, including Regular Spiking (RS), Intrinsically Bursting (IB), and Fast Spiking (FS).

Figure 5: Simulation of a single Izhikevich neuron driven by an external input current. It generates a regular spiking pattern consistent with the Izhikevich (2003) model. The 200 ms time-course of the membrane potential $V_{\{m\}(t)}$ *(upper trace) is shown as the current trajectory (lower trace) switches from (subthreshold) at ms to (exceeding the threshold voltage). The initial membrane potential is set to* $V_{\{rest\}}$.

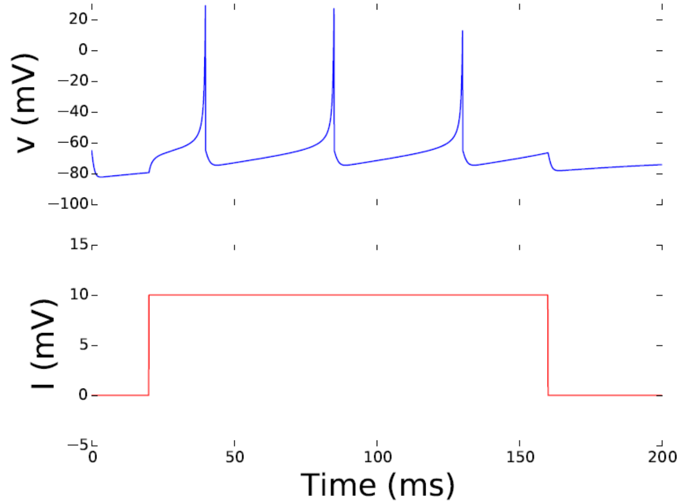

Source: From "Learning spatio-temporal spike train encodings with ReSuMe, DelReSuMe, and Reward-modulated Spike-timing Dependent Plasticity in Spiking Neural Networks," by I. Ozturk, 2017, University of York. Copyright 2017 by I. Ozturk.

Figure 5 demonstrates the dynamic response of the Izhikevich neuron model, which is designed to combine the biological plausibility of Hodgkin–Huxley dynamics with the computational efficiency of integrate-and-fire models. The simulation utilizes a two-dimensional system of ordinary differential equations, where the membrane potential interacts with a recovery variable via a quadratic nonlinearity ($u \leftarrow u + d$) to produce rich firing patterns. As depicted in the 200 ms time-course, the neuron is initially at a resting potential with insufficient input drive (0 mV). At 20 ms, the external current (lower trace) steps to a suprathreshold value (+10), driving the membrane potential (upper trace) to cross the firing threshold. Consistent with the "Regular Spiking" (RS) behavior of cortical neurons described by Izhikevich (2003), the model generates a train of spikes; upon reaching the apex of 30 mV, the voltage is instantaneously reset to a value (typically -65 mV for RS), and the recovery variable is updated ($u \leftarrow u + d$). This phenomenological reset mechanism captures the fast after-hyperpolarization phase, allowing the model to simulate tens of thousands of neurons in real-time while maintaining biophysical fidelity.

- Adaptive Exponential Integrate-and-Fire (AdEx) model represents a significant evolution in phenomenological neuron modelling by augmenting the linear voltage equation with an exponential non-linearity and a second state variable governing adaptation. The exponential term in the differential equation $\tau \frac{dV}{dt} = -(V - V_{rest}) + RI(t)$ mathematically characterizes the rapid, non-linear initiation of an action potential, while the inclusion of the auxiliary adaptation variable (w) allows the system to capture complex temporal dynamics, such as spike-frequency adaptation and initial bursting, which simple integrate-and-fire models fail to reproduce. In a comprehensive analysis, Naud et al. (2008) demonstrated the model's remarkable versatility; by systematically adjusting specific parameters—namely the voltage reset values and the time constant of the adaptation variable w—the AdEx model can accurately reproduce the specific firing patterns of diverse cortical neurons with high biophysical fidelity.

3. Information Encoding and Computation

3.1. Temporal Coding vs. Rate Coding

While second-generation networks rely on a firing rate interpretation, SNNs leverage temporal coding, where information is encoded in the precise timing of individual spikes. This approach is supported by experimental evidence:

Figure 6: Encoding mechanism for the input layer, where neurons (right) receive task-specific spatio-temporal spike patterns. The configuration illustrates the segregation of inputs into two distinct sets, such as for 2-digit binary operations.

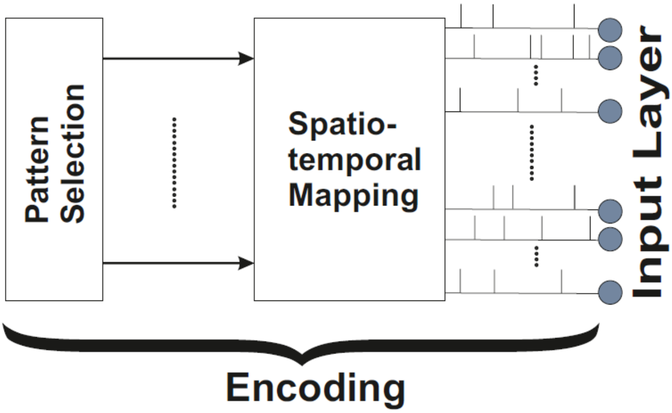

Source: From "Learning spatio-temporal spike train encodings with ReSuMe, DelReSuMe, and Reward-modulated Spike-timing Dependent Plasticity in Spiking Neural Networks," by I. Ozturk, 2017, University of York. Copyright 2017 by I. Ozturk.

- Precision: Shmiel et al. (2005) and Tiesinga et al. (2008) demonstrated that cortical circuits exhibit precise inter-spike timing that correlates with behavior, suggesting that the brain operates with a temporal precision that precludes simple rate-based averaging.

- Synaptic Transmission: Sabatini and Regehr (1999) showed that the timing of synaptic transmission is highly regulated, supporting the feasibility of sub-millisecond temporal codes in biological hardware.

Figure 6 illustrates the encoding mechanism employed at the input layer, serving as the interface where external data is converted into the spike domain. The nodes on the right represent the input layer neurons, which do not receive static numerical values but are instead driven by spatio-temporal patterns of spikes. Based on the pattern selection, a suitable set of spike trains is fed into these input neurons to represent specific data features. For instance, in the context of 2-digit binary operations, the encoding scheme divides the input neurons into two distinct sets, likely corresponding to the two operands. This spatial segregation allows the network to process binary information (0 or 1) through temporal coding—where information is encoded by the precise timing or presence of a spike—enabling the hidden layers to perform computation through mechanisms such as coincidence detection

3.2. Computational Complexity

Theoretically, networks of spiking neurons possess greater computational power than traditional sigmoidal networks. Maass (1997) demonstrated that a single spiking neuron can compute specific functions, such as "Element Distinctness" (determining if a set of real-valued inputs contains distinct values), which would require a significantly larger number of hidden units in a sigmoidal neural network.

3.3. Plasticity and Learning

Computations in SNNs are dynamic, driven by synaptic plasticity. The foundational work of Bliss and Collingridge (1993) on Long-Term Potentiation (LTP) established the synaptic basis for memory. In SNNs, this is often implemented via Spike-Timing-Dependent Plasticity (STDP), where weights are adjusted based on the relative timing of pre- and post-synaptic spikes.

Figure 7: Schematic of the STDP window function illustrating synaptic strength modification based on the temporal difference () between presynaptic () and postsynaptic (Δt) spikes. The curve is derived from experimental data on rat hippocampal neurons.

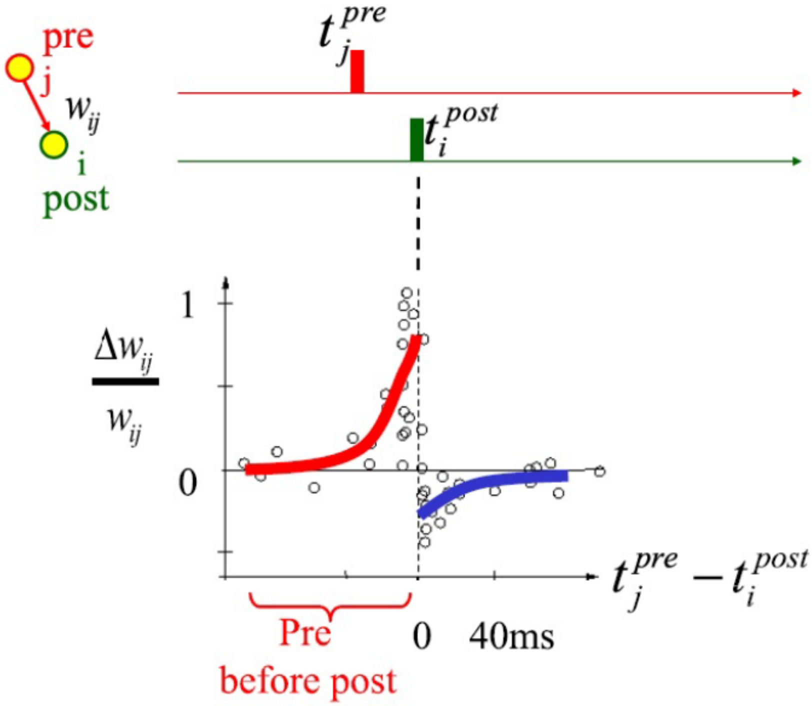

Source: (Bi & Poo, 1998).

Figure 7 illustrates the schematic of the Spike-Timing-Dependent Plasticity (STDP) window function, a fundamental learning rule derived from biological data on rat hippocampal neurons (Bi & Poo, 1998). The graph plots the modification of synaptic efficacy—represented on the vertical axis as a dimensionless change in synaptic strength—against the relative timing (Δt) between presynaptic and postsynaptic spikes. In this specific schematic, the time difference is defined as $\Delta t = t_{pre} - t_{post}$ [Sjostrom & Gerstner (2012)]. The curve demonstrates that the direction and magnitude of weight adjustment (potentiation or depression) are critically dependent on this temporal causality; notably, in the instance of exact coincidence where there is no time difference ($\Delta t = 0$), the model dictates that the synaptic weight remains unchanged ($\Delta w_{ij} = 0$). This dynamic adjustment of weights allows the network to adapt its topology based on the precise timing of input and output activity, a capability essential for temporal pattern learning in biological and artificial systems.

- Delay Selection: Kerr et al. (2013) demonstrated that STDP can select specific delays in recurrent networks. This mechanism allows SNNs to learn temporal patterns by reinforcing pathways that ensure coincident spike arrival, effectively tuning the network's temporal structure.

- Metrics: To quantify learning and information content in these dynamic spike trains, rigorous metrics have been developed, such as those proposed by Rusu and Florian (2014), which measure the distance between spike trains to evaluate encoding precision.

4. Simulation and Tools

The development of SNNs relies on software simulators that vary in their optimization strategies, balancing biological exactness with execution speed. A comprehensive benchmarking study by Kulkarni et al. (2021) evaluated major simulators including NEST, BindsNET, and Brian2.

- NEST: Designed with a focus on biological exactness, NEST excels in simulating large, sparse networks and supports multi-node supercomputing via MPI. It is ideal for complex connectivity tasks but can be hindered by long network loading times.

- BindsNET: Built atop the PyTorch library, BindsNET is optimized for machine learning workloads and leverages GPU acceleration. It demonstrates superior speed for feed-forward and dense architectures.

- Brian2 / Brian2GeNN: Brian2 offers high flexibility, allowing users to define custom differential equations. Its GPU backend, Brian2GeNN, utilizes code generation to outperform other simulators on large, dense networks, where execution time is dominated by simulation rather than data transfer.

5. Conclusion

There is no "one-size-fits-all" approach to modelling and simulating Spiking Neural Networks. The choice of model depends strictly on the application's constraints. For investigations requiring high biological fidelity and complex channel dynamics, the Hodgkin-Huxley model remains the standard. For efficient simulation of large-scale networks that still require realistic firing patterns (such as bursting or adaptation), the AdEx model (Naud et al., 2008) or Izhikevich model are preferred. Future research focuses on integrating these models with plasticity rules (Kerr et al., 2013) to develop general-purpose simulators that balance ease of programmability with the scalability required for massive neuromorphic evaluations.

6. Bibliography

Bliss, T. V. P., & Collingridge, G. L. (1993). A synaptic model of memory: long-term potentiation in the hippocampus. Nature, 361, 31–39.

Gerstner, W., & Kistler, W. M. (2002). Spiking neuron models: single neurons, populations, plasticity. Cambridge University Press.

Hodgkin, A. L., & Huxley, A. F. (1952). A quantitative description of membrane current and its application to conduction and excitation in nerve. The Journal of Physiology, 117(4), 500-544.

Izhikevich, E. M. (2003). Simple model of spiking neurons. IEEE Transactions on Neural Networks, 14(6), 1569-1572.

Kerr, R. R., Burkitt, A. N., Thomas, D. A., Gilson, M., & Grayden, D. B. (2013). Delay selection by spike-timing-dependent plasticity in recurrent networks of spiking neurons receiving oscillatory inputs. PLoS Comput. Biol., 9(2), e1002897.

Kulkarni, S. R., Parsa, M., Mitchell, J. P., & Schuman, C. D. (2021). Benchmarking the Performance of Neuromorphic and Spiking Neural Network Simulators. Neurocomputing.

Maass, W. (1997). Networks of spiking neurons: the third generation of neural network models. Neural Networks, 10(9), 1659-1671.

Naud, R., Marcille, N., Clopath, C., & Gerstner, W. (2008). Firing patterns in the adaptive exponential integrate-and-fire model. Biol Cybern, 99(4–5), 335–347.

Ozturk, I. (2017). Learning spatio-temporal spike train encodings with ReSuMe, DelReSuMe, and Reward-modulated Spike-timing Dependent Plasticity in Spiking Neural Networks [Unpublished doctoral dissertation]. University of York.

Rusu, C. V., & Florian, R. V. (2014). A new class of metrics for spike trains. Neural Comput, 26(2), 306–348.

Sabatini, B. L., & Regehr, W. G. (1999). Timing of synaptic transmission. Annual Review of Physiology, 61(1), 521–542.

Shmiel, T., Drori, R., Shmiel, O., Ben-Shaul, Y., Nadasdy, Z., Shemesh, M., Teicher, M., & Abeles, M. (2005). Neurons of the cerebral cortex exhibit precise interspike timing in correspondence to behavior. Proc. Natl. Acad. Sci. U.S.A., 102(51), 18655–18657.

Stimberg, M., Goodman, D. F., & Nowotny, T. (2020). Brian2GeNN: accelerating spiking neural network simulations with graphics hardware. Scientific Reports, 10(1), 1-12.

Tiesinga, P., Fellous, J. M., & Sejnowski, T. J. (2008). Regulation of spike timing in visual cortical circuits. Nat. Rev. Neurosci., 9(2), 97–107.

CHAPTER 4

FLUX PINNING MECHANISMS OF SUPERCONDUCTING SAMPLES SUBSTITUTED WITH DIFFERENT RATIOS OF NANO-SIZED Eu TO STRONTIUM SITES

1. MEHMET ERSİN AYTEKİN [1]

INTRODUCTION

Superconductivity was first discovered in 1911 by H. Kamerlingh Onnes when the electrical resistance of mercury dropped to zero at a temperature of 4.2 K. This discovery paved the way for intensive research into understanding the physical mechanisms of low-temperature superconductors, and in 1957, the Bardeen–Cooper–Schrieffer (BCS) theory successfully explained the microscopic origin of superconductivity (Bardeen, Cooper, & Schrieffer, 1957). The critical temperature (*Tc*) of conventional superconductors, which were the earliest superconducting systems, was generally around 30 K. Conventional superconducting materials required liquid helium systems capable of reaching temperatures below 30 K to achieve superconductivity. Liquid helium systems were complex and costly for the use of conventional

---

[1] Asst. Prof., Tarsus University, Department of Electronics and Automation, Mersin, Türkiye Orcid: 0000-0003-0731-

superconductors in zero resistance and magnetization applications. Researchers focused on systems that could exhibit superconducting properties at higher temperatures (liquid nitrogen temperatures). In 1986, the research conducted by Bednorz and Müller, which achieved superconductivity at around 35 K in the La–Ba–Cu–O system, marked a turning point in the field of superconductivity. This led to the discovery of a new class of materials known as 'high-temperature superconductors” (HTS) (Bednorz & Müller, 1986). Moreover, this discovery led to the era of the copper-oxide (cuprate) based high-temperature superconductor family, and within a short time, critical temperatures were raised above liquid nitrogen temperature (77 K). In particular, achieving a *Tc* value of 92 K in the $YBa_2Cu_3O_7-\delta$ (Y-123) system has significantly increased the technological feasibility of high-temperature superconductors.

High-temperature superconductors generally have a layered crystal structure, and superconductivity occurs in the CuO_2 planes. These materials are classified into different families depending on their crystal structure, chemical composition, and number of layers. The main copper oxide-based high-temperature superconductor families are Bi-Sr-Ca-Cu-O (BSCCO), Tl-Ba-Ca-Cu-O (TBCCO), Hg-Ba-Ca-Cu-O (HBCCO), Y-Ba-Cu-O (YBCO), and La-Sr-Cu-O (LSCO) systems (Humaidi, 2020).

Bismuth-based high-temperature superconductors (BSCCO) containing Bi–Sr–Ca–Cu–O elements are among the intensively researched systems due to their high critical temperatures, layered crystal structures, and relatively easy synthesis (de Vera, Bardolaza, Arcilla, & Sarmago, 2019). The BSCCO family contains the $Bi_2Sr_2CuO_6+\delta$ (Bi-2201) and $Bi_2Sr_2CaCu_2O_{10}+\delta$ (Bi-2223) phases, which differ based on the number of CuO_2 planes. $Bi_2Sr_2CaCu_2O_8+\delta$ (Bi-2212), and $Bi_2Sr_2Ca_2Cu_3O_{10}+\delta$ (Bi-2223) phases, which have critical temperatures of approximately 20 K, 85 K, and 110 K, respectively (Guner et al., 2019). As all copper oxide layered superconducting systems, BSCCO superconductors have a layered crystal structure exhibiting strong structural anisotropy. In copper oxide-based high-temperature systems, it is well known that the superconductivity mechanism occurs within the CuO_2 planes, while the other layers act as charge reservoirs (Yamauchi & Karppinen, 1998). Among BSCCO superconducting systems, the Bi-2212 phase's critical temperature (*Tc*) of approximately 85–90 K, allowing it to operate with liquid nitrogen or cryogenic cooling systems, increases Bi-2212's attractiveness in practical applications. Furthermore, the Bi-2212 phase is central to research and development efforts due to its relatively low anisotropy, chemical stability, and ease of conversion into wire/tape form (Frank et al., 2003).

Bi-2212 superconductors are widely used in high-field magnets and superconducting wires. The ability to produce Bi-2212 in a round-section wire form is a significant advantage that distinguishes it from other cuprate superconductors (Özkurt, 2014). Furthermore, Bi-2212 superconducting systems, due to their high phase stability, are candidate materials for applications requiring high and homogeneous magnetic fields, such as particle accelerators, nuclear magnetic resonance imaging (NMR), and magnetic resonance imaging (MRI) systems (Aytekin, Akyol, & Özkurt, 2024).

According to BCS theory, the phenomenon of superconductivity is based on the formation of paired 'Cooper pairs' resulting from the interaction of conductive electrons at low temperatures. In conventional superconductors, two electrons with opposite spins and momentum can pair up near the Fermi surface via electron-phonon interactions. Unlike single electrons, these pairs exhibit a quantum state resistant to scattering, causing the electrical resistance to drop to zero. As a result, the material exhibits zero electrical resistance (R = 0).

The formation mechanism of Cooper pairs in high-temperature superconductors is more complex compared to conventional superconductors. The strong electron correlations, low-dimensional layered crystal structure, and pronounced electronic anisotropy observed particularly in copper oxide (cuprate)-based superconductors make it insufficient to explain superconductivity solely through electron-phonon interactions (Anderson, 1987). In this context, it is widely accepted that spin fluctuations and magnetic interactions play a decisive role in the binding mechanism of Cooper pairs (Scalapino, 1995). Nevertheless, the superconducting state observed in high-temperature superconductors is still thought to be associated with the formation of Cooper pairs and their movement in a long-range pattern along the CuO_2 planes (Tsuei & Kirtley, 2000). The mobility of Cooper pairs within the crystal structure is strongly influenced by microstructural factors such as carrier density, oxygen content, and grain boundary characteristics. Weak connections formed at grain boundaries can disrupt the continuity of Cooper pairs, leading to a decrease in critical current density. In high-temperature superconductors, the stable movement of Cooper pairs is directly related to the improvement of structural order and grain boundary coupling. In BSCCO superconducting systems, as in copper oxide-based high-temperature superconducting families, the morphological structure, grain arrangement, interphase junctions, and impurity phases hinder the movement of paired electrons. Therefore, for advanced applications requiring high magnetic capacitance, high-speed energy transfer, and high current density, Bi-2212 superconducting systems with more homogeneous morphological structure and phase characteristics should be developed. The literature widely discusses nanoparticle substitution as an effective approach for improving the microstructural and electrical properties of Bi-2212 superconductors. Several studies have reported that the substitution of nanoparticles promotes grain growth, reduces porosity and contributes to the formation of stronger, more homogeneous bonds between grains during sintering (Zelati, Amirabadizadeh, Kompany, Salamati, & Sonier, 2014). In addition, by being positioned at the grain boundaries of nanoparticles, they strengthen the regions that are weak links and contribute to the movement of carrier mechanisms (Agail & Abd-Shukor, 2014; S. Zhang et al., 2015). Optimal nanoparticle doping enhances electrical continuity between CuO_2 planes by suppressing secondary phase formation, thereby facilitating intergranular superconducting current transfer. These microstructural improvements result in higher critical current density *(Jc)*, a sharper superconductivity transition (ΔTc), and improved magnetic properties.

In a Bi-2212 system belonging to the Type-II superconductor class, magnetic fluxes (or vortices) can penetrate the superconducting matrix when the externally applied magnetic field exceeds the subcritical area (H_{c1}), and the movement of these vortices under external influences leads to energy losses and degradation of diamagnetic properties (Albiss, Obaidat, Gharaibeh, Ghamlouche, & Obeidat, 2010). Therefore, it is crucial to prevent vortex movements in order to maintain the current-carrying performance of superconducting materials. The most important method for preventing vortex movements is to create flux pinning centers within the crystal structure (Abbas, Abdulridha, & Jassim, 2017). The formation of effective flux-pinning centres in Bi-2212 superconductors is directly related to the material's microstructural properties. Natural defects such as grain boundaries, secondary phases, dislocations, and oxygen irregularities are considered potential centers playing a role in the pinning of vortices (Humaidi, 2020).

Factors such as the irregular distribution of grains, the non-homogeneous phase structure, and poor pinning performance cause *Jc* to decrease rapidly, especially at high magnetic fields. Creating controlled and homogeneous flux pinning centres is an effective strategy for improving the performance of Bi-2212-based superconductors in high magnetic fields. Nano-sized particle doping is reported as one of the most common and effective methods for creating artificial flux pinning centers in Bi-2212 superconductors (Hernández-Wolpez et al., 2020). The incorporation of nano-sized elements and compounds, such as gold (Au), cobalt oxide (Co_3O_4), bismuth ferrite ($BiFeO_3$), tin oxide (SnO_2) and zirconium oxide (ZrO_2), into the crystal structure of BSCCO superconductors at sizes close to the coherence length (approximately 3 nm) improves the Jc performance of the BSCCO system by acting as flux pinning centre(Aytekİn, 2024a; Öztornacı & Özkurt, 2017). In a previous study, the superconductivity properties of the $Bi_2Sr_{2-x}Eu_xCa_1Cu_2O_y$ (x=0.00, 0.05, 0.1, and 0.2) system were investigated. The findings reported that the superconducting properties were enhanced by substituting with Eu at a nano-sized of x = 0.1 (Aytekin, 2025a). In the presented study, the flux pinning performance of nano-sized Eu substituting in the Bi-2212 superconducting system was evaluated.

EXPERIMENTAL

Many research groups prefer to synthesise Bi-2212 ceramic superconductors using the solid-state reaction method because it is easy and cost-effective. In this method, high-purity starting powders based on oxides or carbonates are weighed in proportions suitable for the target stoichiometry and mechanically ground until a homogeneous mixture is obtained. The resulting mixture is subjected to controlled heat treatments, including intermediate calcination steps, to initiate the formation of the superconducting phase and remove unwanted components. In the solid-state reaction method, repeated grinding and heat treatment cycles applied in the material production process increase phase homogeneity and degree of crystallization. During the final sintering stage, grain growth and intergranular bonding mechanisms become active, thereby improving the microstructural integrity of the ceramic samples. Furthermore, the sintering atmosphere and cooling conditions directly affect the oxygen content in Bi-2212 superconductors, playing a decisive role in tuning the superconductivity transition temperature (*Tc*) and electrical properties. The solid-state reaction method is one of the most widely used methods in the literature for the preparation of Bi-2212 ceramic superconductors due to its ease of application, cost-effectiveness, and ability to produce large volumes of samples. The production and characterization processes of $Bi_2Sr_{2-x}Eu_xCa_1Cu_2O_y$ (x=0.00, 0.05, 0.1, and 0.2) ceramic superconductors via solid-state reaction method are described in detail (Aytekin, 2025a). This study aims to determine the flux pinning properties of the $Bi_2Sr_{2-x}Eu_xCa_1Cu_2O_y$ (x = 0.00, 0.05, 0.1 and 0.2) systemTo explain the characterization findings of the samples, they were named according to their nano-sized Eu contribution as follows: Sample A = 0.0, Sample B = 0.05, Sample C = 0.1, and Sample D = 0.2.

RESULTS

To characterize the physical, superconductivity, and magnetic properties of nano-sized (80 nm) Eu-substituted Bi-2212 high-temperature ceramic materials, X-ray diffraction, morphological, superconductivity, and magnetic measurements were performed, respectively.

X-ray diffraction (XRD) measurements were performed to determine the phase structures of Bi-2212 superconducting samples. These measurements were carried out by directing X-rays onto the Bi-2212 superconducting samples at a specific angle. X-rays impacting the sample diffract from the crystal planes according to Bragg's law, and these diffractions are recorded by the detector as a function of the 2θ angle.The obtained diffraction patterns provide information about the Bi-2212 superconducting phases and impurity phases formed in the material. X-ray diffraction measurements of ceramic superconducting samples are shown in Figure 1.

Figure 1 Phase characterization results of Bi-2212 ceramic samples (Aytekin, 2025a)

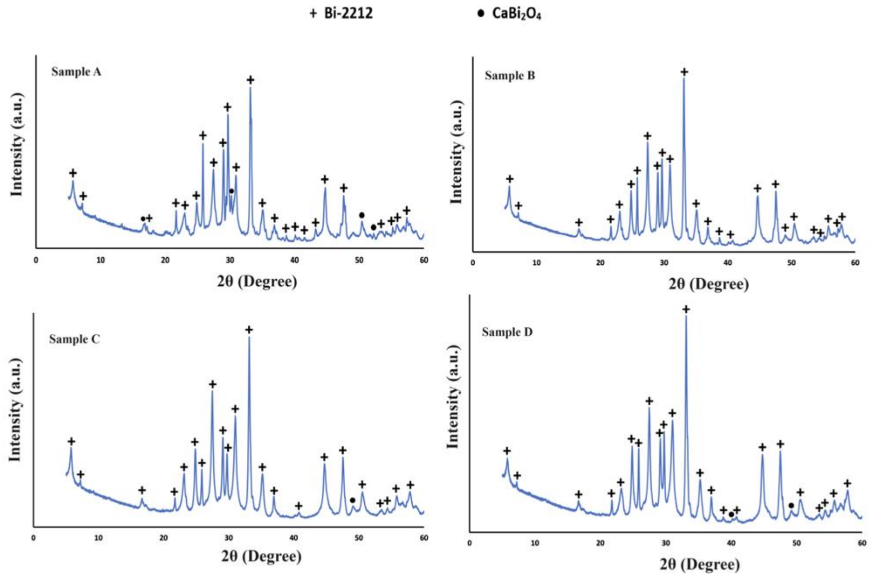

In the X-ray diffraction results, the + symbol represents the Bi-2212 high-temperature superconducting phase, and the ● symbol represents the $CaBi_2O_4$ impurity phase. Although the phase analysis results of all samples showed the formation of minor amounts of impurity phases, the basic phase structure is the Bi-2212 superconducting phase. The presence of the Bi-2212 high-temperature phase as the dominant phase in the ceramic samples may suggest that they will exhibit superconducting behaviour. However, changes in phase behaviour were observed at different ratios of nanosized Eu substitution.

Phase analysis in Bi-2212 superconductors is one of the most important structural parameters that directly affects the superconductivity performance of the material. An increase in non-superconducting secondary phases within the crystal structure results in weaker bonds at grain boundaries, which limits the flow of carriers (Cooper pairs) These negative effects weaken fundamental superconductivity characteristics such as magnetic performance, critical current density (*Jc*), and superconductivity transition temperature (*Tc*) (Özkurt, 2012). In contrast, obtaining a highly crystallized and well-crystallized Bi-2212 phase results in sharper superconducting transitions due to improved interconnections between intragranular and intergranular superconducting phases. As shown in Figure 1, the addition of nano-sized Eu to the system resulted in a reduction in the number of impurity phases. Furthermore, in sample C containing nano-sized Eu at a ratio of x = 0.1, in addition to the reduction in impurity phases, there was an increase in the intensity of the characteristic peaks of the Bi-2212 phase. These developments may indicate improvements in the homogeneous phase structure of the material and the formation of strong bonds between superconducting phases. Improvements in superconductivity properties can be expected in the case of sample C due to these phase improvements.

Morphological properties of high-temperature ceramic superconductors, as well as their phase structures, are among the fundamental microstructural parameters that determine their superconductivity performance (Kocabas, Özkan, Bilgili, Kadıoglu, & Yılmaz, 2010). These materials generally exhibit a layered and plate-like grain morphology. The intergranular transfer of carriers (Cooper pairs) is directly influenced by grain size, grain orientation, grain boundary structure and porosity ratio, and these factors play a decisive role in determining the critical current density (*Jc*) and the sharpness of the superconductivity transition (Şakiroğlu & Kocabaş, 2011). Techniques such as synthesis method, sintering temperature and time, and nano-sized doping promote grain growth, strengthen grain boundary connections, and achieve a more compact morphological structure, thereby improving the superconductivity performance of the material. These advancements also promote the technological applicability of Bi-2212 superconductors.

SEM measurements were performed to characterize the morphological properties of samples containing varying concentrations of nano-sized Eu susbtution. Morphological images obtained by SEM measurement are shown in Figure 2.

Figure 2 SEM results of nano-sized Eu-substituted samples

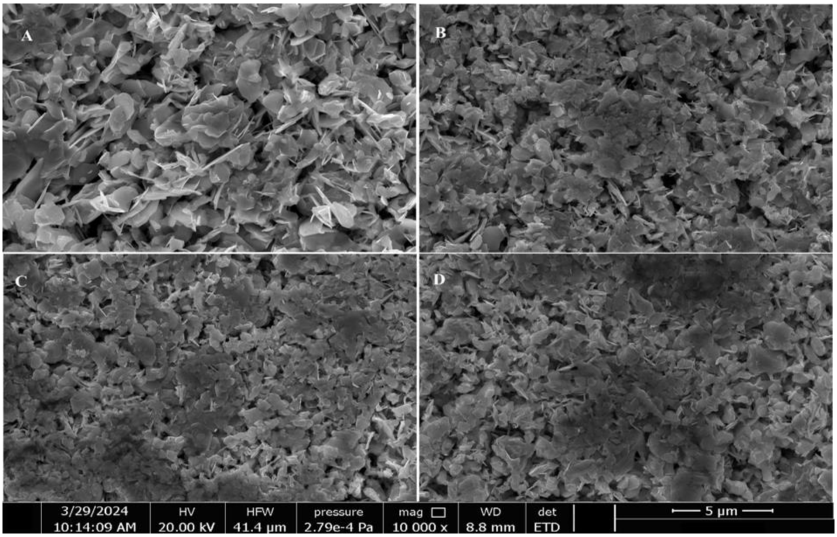

Plate-like grains separated by grain boundaries are a characteristic morphological behavior of Bi-2212 high-temperature superconductors (Bilgili, 2021; Nurbaisyatul, Azhan, Kasim, & Ibrahim, 2020). As seen from the SEM results of the samples, the morphological structure of all samples consists of plate-like grains that form gaps between them and are separated from each other by grain boundaries, consistent with the X-ray measurement results. Furthermore, some morphological modifications occurred as a result of substituting nano-sized Eu at different ratios.

As seen in Figure 2, sample A, which does not contain Eu substitution, exhibits voids between plate-like grains and a random orientation of the grains. With the addition of nano-sized Eu substitution, the random orientation behavior in the grains gradually decreasesFurthermore, a reduction in the porous structure and strengthened intergranular connections are observed, indicating that nano-sized Eu particles can fill the spaces between the grains. Morphological modifications, such as stronger bonding of grains at fewer grain boundaries and large plate-like grains, can enhance the stability of the superconducting system and improve performance at high magnetic fields.

Resistivity-temperature measurements were performed to characterize the electrical properties of superconducting samples doped with different ratios of nano-sized Eu particles. These measurements were performed using a Physical Property Measurement System (PPMS), which offers high accuracy and a wide temperature range. Four electrical contacts (typically silver-painted or gold-plated) are linearly placed on the sample surface and connected to the PPMS measurement system, and the resistivity is calculated via current-voltage (I-V) measurements. Ceramic superconducting samples are screened in the temperature range of 150 K–10 K (or lower) by controlled cooling via a PPMS cryostat system. While resistivity in the normal conductive phase decreases with temperature, a sudden drop in resistivity occurs as the superconducting transition temperature (Tc) is approached, and ideally, zero resistivity is reached. Two different transition temperatures are observed in superconductors. T_c^{onset} is defined as the temperature at which transitions from the normal phase to the superconductor begin and is associated with the formation of superconducting phases (Aytekin & Akyol, 2024). T_c^{offset} temperature is the temperature at which superconductivity transitions are completed and zero resistance begins in the material. The temperature at which the T_c^{offset} is related to the quality of the interphase junction (Aytekin, 2025b). The difference between the two temperatures is called ΔTc and is related to the homogeneous phase structure of the material (AYTEKİN, 2024b).

In BSCCO ceramic superconductors, the high density and intensity of the superconducting phases and the minimal presence of secondary phases lead to improved superconductivity transition temperatures. On the other hand, morphological irregularities, weak bonding at grain boundaries, and porous structures can interrupt superconducting current paths, leading to interruptions in superconducting transitions (Ulgen, Turgay, Terzioglu, Yildirim, & Oz, 2018).

The superconductivity transition temperature values of samples containing different ratios of nano-sized Eu substituting are shown in Table 1.

Table 1 Superconductivity transition temperature values of superconducting samples (Aytekin, 2025a)

Substution Value	Sample	T_c^{onset} (K)	T_c^{ofset} (K)	ΔTc (K)
0.0	Sample A	82.33	45.45	36.88
0.05	Sample B	87.07	53.11	33.96
0.1	Sample C	90.50	57.56	32.94
0.2	Sample D	44.23	27.88	16.35

As shown in Table 1, the values of the superconductivity transition temperature change with nano-sized Eu substitution in ceramic superconducting samples. As previously discussed, the substitution of nano-sized Eu alters the phase formation mechanisms in the samples. Increasing Eu substitution in the morphological structure was detected alongside modifications in the properties of the particles.

Poor formation of a stable phase structure, weak coupling between high-temperature superconducting phases and the creation of barriers between superconducting regions by impurity phases can lead to the scattering of paired electrons. This situation leads to fluctuations in superconducting transitions and a delay in the zero-resistance properties.

In agreement with the X-ray measurement results, an increase in the superconducting temperature was observed as the level of nano-sized Eu substitution increased ($x < 0.2$). Furthermore, improving the granular properties of the morphological structure increased the superconductivity transition temperature value with nano-sized Eu substituting at a ratio of up to 0.2. High superconductivity transition temperatures were observed in the C sample containing nano-sized Eu at a ratio of $x = 0.1$, depending on parameters such as homogeneous phase formation, increases in the intensities of characteristic phases, and the formation of strong intergranular bonds. In sample D, which contains the maximum susbtitution, the superconductivity performance deteriorated with the decrease in the density of the Bi-2212 superconducting phase.

M-H characterization was performed on a PPMS measurement system to determine the magnetic performance of ceramic samples. This characterization method allows for the analysis of parameters such as the magnetic behavior, flux pinning properties, and critical current density of Bi-2212 high-temperature superconductors.

Magnetic measurements with PPMS are performed by keeping the sample temperature constant at a desired value, increasing the magnetic field from zero to a maximum value, and then applying the same magnetic field in the reverse direction. The magnetic field is scanned across the material in different vector directions until the target value is reached. During this field scan, the magnetization (M) of the ceramic superconducting sample is obtained as a function of the applied magnetic field (H), and M–H hysteresis curves are plotted. The magnetic-h (magnetization-magnetic field) performance of Bi-2212 ceramic superconductors, grain size and grain boundary junction quality, and strong bonds between superconducting phases play a decisive role in magnetic hysteresis behavior (Kır, Özkurt, & Aytekin, 2016). To improve magnetic transport properties, the hysteresis field needs to be expanded. In addition, the geometry of the hysteresis field must be uniform (Z. Zhang et al., 2024). However, homogeneous crystalline properties and the formation of homogeneous high-temperature phases can lead to hysteresis behavior in regular geometry and symmetry.

In addition to their zero-resistance property, superconductors also possess strong diamagnetic properties, making them promising for technological applications. Materials with high magnetic field carrying capacity (*Hc*) are a necessary feature in developing technology. Significant progress has been made in improving diamagnetic properties as well as electrical properties in ceramic superconductors. In particular, nano-sized element substituting contributes to the enhancement of magnetic moments, improving the magnetic properties of the system.

The M-H hysteresis graphs obtained in ceramic samples at temperatures of 15 K and 25 K and a magnetic field of ± 20000 Oe are shown in Figures 3 and 4, respectively.

Figure 3 M-H hysteresis graph of samples containing different ratios of Eu nanoparticles at 15 K (Aytekin, 2025a)

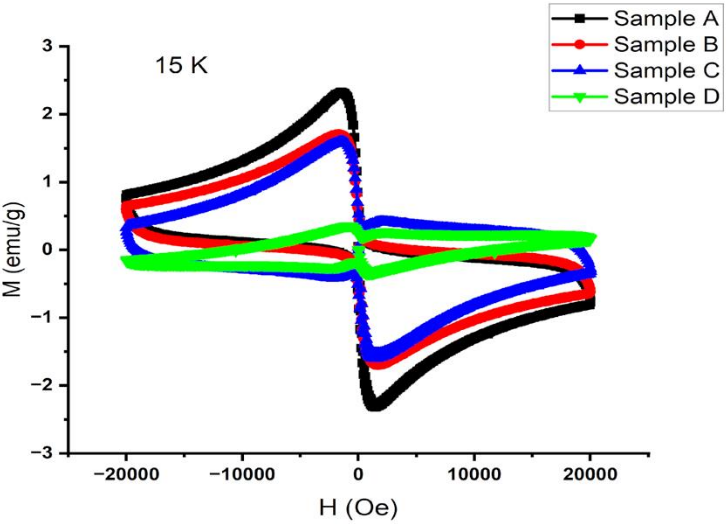

Figure 4 M-H hysteresis graph of samples containing different ratios of Eu nanoparticles at 25 K (Aytekin, 2025a)

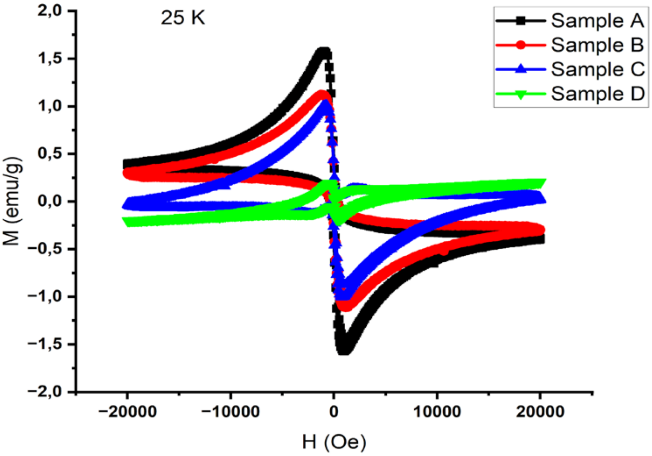

In the M-H measurement results obtained at both temperatures, a hysteresis closed-loop graph, which is the characteristic behavior of Bi-2212 superconductors, was observed. Furthermore, the formation of superconducting phases at optimum levels and the presence of plate-like grains in the morphological structure indicate the occurrence of closed-loop hysteresis behavior in a regular geometry. Additionally, changes in magnetic properties were indicated by differences in the hysteresis field, which occurred at varying ratios of nano-sized Eu substitution.

In BSCCO superconducting systems, the magnetisation results are dependent on morphological properties such as grain size, grain boundary junction quality and porosity []. Furthermore, second-phase formations, nanosized doping, and defect structures contribute to the expansion of the M–H loop and increased magnetic stability at high fields by creating effective flux pinning centers (Aytekin & Akyol, 2024). Magnetization measurements performed at both temperatures show that nano-sized Eu particles with a ratio of $x = 0.1$ contribute to the enhancement of magnetic properties. In sample C, the high formation of superconducting phases and optimum crystallization, along with the formation of uniformly distributed and strongly bonded grains in the morphological structure, lead to the development of a hysteresis zone. In sample D, which contains higher nano-sized Eu substitution, although there were no significant changes in the morphological structure, the magnetic properties weakened due to the decrease in the Bi-2212 superconducting phase density in the phase structure.

The ΔM values obtained from the M–H measurements were used to calculate the critical current density (*Jc*) using the Bean critical state model. The following formula was used in the calculations (Bean, 1962).

$$Jc = 30\,(\Delta M/d)$$

The intergranular magnetization current density, expressed in amperes per square centimeter, is marked by Jc. Measured in electromagnetic units per cubic centimeter, $\Delta M = M+ - M-$. The sample's thickness is denoted by d.

The Bean critical current model is an effective approach widely used in determining the critical current density of Bi-2212 ceramic high-temperature superconductors from magnetic measurements. In Bi-2212 systems, intergranular current transport predominates at low magnetic fields, while intragranular current transport predominates at high magnetic fields, and this is reflected in the magnetic field dependence of *Jc* (Özçelik, Ergin, Madre, & Sotelo, 2020). Therefore, the *Jc* values obtained with the Bean model provide important information for evaluating the effects of flux pinning efficiency and grain boundary junctions on superconductivity performance (Verma, Kaipamangalath, Varma, & Bai, 2023).

In BSCCO ceramic high-temperature superconductors, the critical current density is strongly dependent on the microstructural (morphological), phase system characteristics, and magnetic properties of the material. Specifically, grain size and grain boundary relationships play a decisive role in *Jc*, with weakly coupled or high-angle grain boundaries causing scattering of the superconducting current, thus reducing the *Jc* value. However, phase purity and the ratio of the target superconducting phase are also critical; the presence of secondary phases restricts current transport paths, reducing the critical current density. Therefore, in order for these materials to be used in transmission elements with the current capacity required by developing technologies, improvements in morphological and phase structure must be made to achieve high *Jc* values. The most important solution for achieving these improvements is the addition of nanoparticles of appropriate size into the material.

The *Jc* values, theoretically calculated from magnetization measurements using Bean's model, are shown in Figures 5 and 6 for temperatures of 15 K and 25 K, respectively.

Figure 5. Jc graph of ceramic properties at 15 K temperature, theoretically calculated from the Bean model (Aytekin, 2025a)

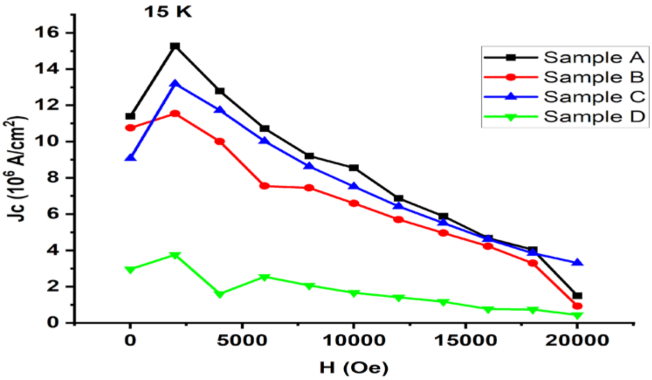

Figure 6 Jc graph of ceramic properties at 25 K temperature, theoretically calculated from the Bean model (Aytekin, 2025a)

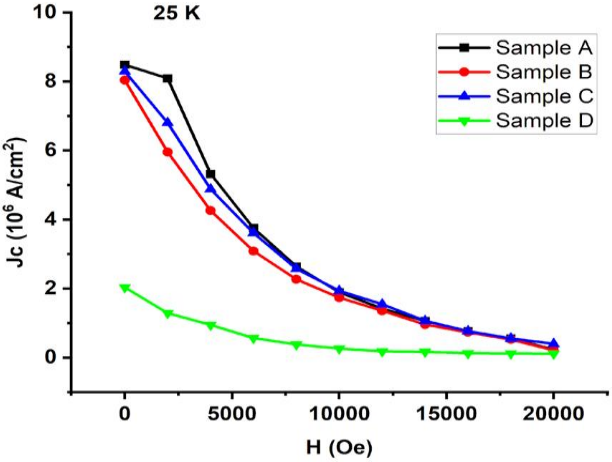

As seen in Figures 5 and 6, changes in the Jc value were observed due to morphological and phase structural changes with nano-sized particle substitution. The formation of plate-like grains in the surface structure at an optimum ratio and the predominance of Bi-2212 phases in the sample, which does not contain nano-sized Eu particles, explains the overall diamagnetic behavior. In the Jc results obtained from magnetic measurements, higher Jc values are observed in the low magnetic field regions in sample A, which is consistent with other measurements. These results also suggest that the material has poor flux pinning capability. Compared to other examples, a high critical current density was obtained in sample C due to the development of grain linkages in the morphological structure and the increase in intensities in the characteristic phases. Also high Jc values may indicate optimum flux pinning capasities.

Flux pinning mechanisms in Bi-2212-based ceramic high-temperature superconductors are one of the key factors determining superconductivity performance under a high magnetic field. The movement of magnetic flux vortices entering a superconductor under an applied magnetic field leads to energy losses and a decrease in the Jc value. To maintain the superconducting current performance of the material, the vortices must be effectively pinning. This vortex pinning is only possible through flux pinning centersThe layered and anisotropic crystal structure of Bi-2212 systems results in limited natural flux pinnnig centers, making the creation of artificial pinnnig centers of extremely importance. While point defects and dislocations within the crystal structure act as natural flux pinning centres, microstructural irregularities created by nanoscale secondary-phase doping, foreign-atom substitution and controlled heat treatment processes form effective artificial flux pinning centre []. In particular, it has been reported that nanoparticle doping suppresses vortex motion by creating defects at scales close to the vortex core size, thereby contributing to the maintain of *Jc* values even in high magnetic fields (Vu et al., 2023). Therefore, optimizing the density, distribution, and efficiency of flux pinning centers in Bi-2212 superconducting systems is a critical strategy for achieving high critical current density and magnetic field stability.

To investigate the effect of different ratios of nano-sized Eu particles on flux pinning properties, calculations of flux pinning force were performed from the formula Fp = Jc X B (2). (Tran et al., 2019; Wang, Wang, & Wang, 2023). The graphs showing the flux pinning force calculated at 15 K and 25 K temperatures are shown in Figures 7 and 8, respectively.

Figure 7 Flux pinning force graph of ceramic properties at 15 K temperature

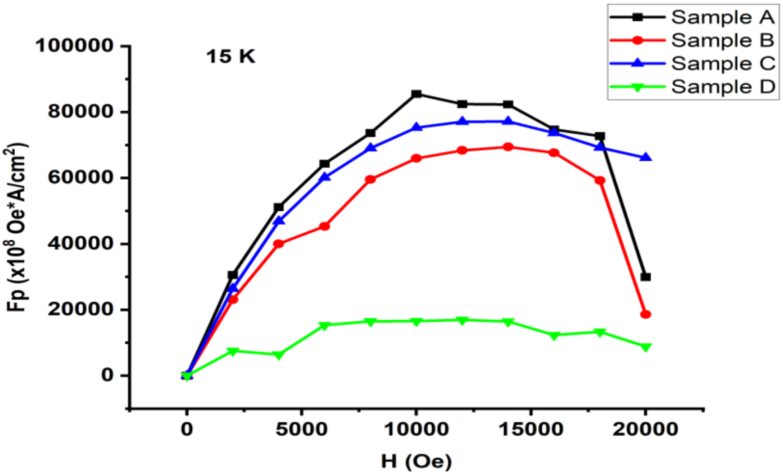

Figure 8 Flux pinning force graph of ceramic properties at 25 K temperature

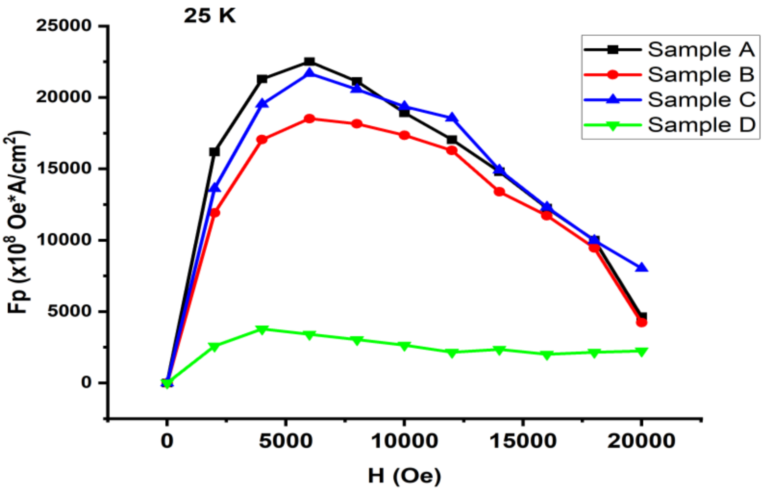

In sample A, which does not contain Eu nanoparticle, the homogeneous distribution of plate-like grains in the morphological structure resulted in the formation of optimum flux pinning centre and a high *Fp* force. In example B, the nano-sized Eu particles did not contribute sufficiently to the formation of flux pinning centers, resulting in a lower Fp value compared to the undoped example. In the sample C, the formation of flux pegging centres was increased by the presence of Eu nanoparticles, which also increased the net Fp. The high Fp value, particularly at temperatures of 25 K and in magnetic fields of 20,000 Oe, suggests the development of more stable magnetic properties. In the sample D, the weakening of superconducting regions weakens the coupled electron mechanisms, resulting in a weakening of both electrical and magnetic properties.

In summary, the presented study involves substituting the strontium regions in the $Bi_2Sr_2Ca_1Cu_2O_y$ system with different ratios of 80 nm Eu particles (x=0.00, 0.05, 0.1, and 0.2). The findings show that Eu nanoparticles with a ratio of x = 0.01 contributed to the formation of the Bi-2212 superconducting phase, increasing both the density of the Bi-2212 superconducting phase and the intensity of the characteristic peaks. In the morphological structure, strong bonds have formed between the wide plate-like grains with an x = 0.1 substitution. With improvements in phase structure and morphological structure, the superconductivity transition temperature (onset) was increased from 82.33 K to 90.50 K with a nano-sized Eu particle of x = 0.1 (Aytekin, 2025a). On the other hand, at a temperature of 15 K, with the substitution of x = 0.1 Eu particles and physical and morphological modifications, and in the presence of a flux pinning force of Fp = 6.612 x 10^8, an improved Jc value of 4.012 × 10^6 A/cm^2 was obtained.

ACKNOWLEDGE

This study utilizes data from the article “Modification of the electrical and magnetic properties of Bi-2212 ceramic superconductors by nano-sized europium substitution.” The M-H and Jc data from the same article were used for flux pinning center interpretation.

REFERENCES

Abbas, M., Abdulridha, A., & Jassim, A. (2017). Effect of Ti Nanoparticles on (Bi, Pb)-2223, Superconducting Thin Films. *Digest journal of nanomaterials and biostructures, 12*(4), 1049-1055.

Agail, A., & Abd-Shukor, R. (2014). Effect of nano-size SnO2 addition on (Bi, Pb)-Sr-Ca-Cu-O superconductor. *Solid State Science and Technology, 22*(1), 2.

Albiss, B., Obaidat, I., Gharaibeh, M., Ghamlouche, H., & Obeidat, S. (2010). Impact of addition of magnetic nanoparticles on vortex pinning and microstructure properties of Bi–Sr–Ca–Cu–O superconductor. *Solid State Communications, 150*(33-34), 1542-1547.

Anderson, P. W. (1987). The resonating valence bond state in La2CuO4 and superconductivity. *science, 235*(4793), 1196-1198.

Aytekin, M. E. (2025a). Modification of the electrical and magnetic properties of Bi-2212 ceramic superconductors by nano-sized europium substitution. *Journal of Materials Science: Materials in Electronics, 36*(29), 1870.

Aytekin, M. E. (2025b). Superconductivity Properties of Bi-2223 Ceramics Substituted with Strontium Sites at Large Scale Nano-Sized Europium Nanoparticles. *Journal of NanoScience in Advanced Materials, 4*(2), 67-75.

Aytekİn, M. E. (2024a). Change in Physical, Electrical and Magnetic Properties of Bi-2212 Superconducting Materials Co-Substituted with Nano-Sized Zinc and Sodium. *Transactions on Electrical and Electronic Materials*, 1-13.

AYTEKİN, M. E. (2024b). The role of post-annealing process on the physical, electrical and magnetic properties of nano-sized tin substituted Bi-2212 superconducting ceramics. *Journal of Materials Science: Materials in Electronics, 35*(28), 1854.

Aytekin, M. E., & Akyol, M. (2024). Effect of nano-sized europium substitution on strontium sites on diamagnetic properties in BiPb-2223 superconductor system. *Journal of NanoScience in Advanced Materials, 3*(1), 8-14.

Aytekin, M. E., Akyol, M., & Özkurt, B. (2024). Improvement in electrical properties of Bi-2212 superconducting materials substituted with large-scale nano-sized tin. *Applied Physics A, 130*(2), 78.

Bardeen, J., Cooper, L. N., & Schrieffer, J. R. (1957). Microscopic theory of superconductivity. *Physical Review, 106*(1), 162.

Bean, C. P. (1962). Magnetization of hard superconductors. *Physical review letters, 8*(6), 250.

Bednorz, J. G., & Müller, K. A. (1986). Possible high T c superconductivity in the Ba− La− Cu− O system. *Zeitschrift für Physik B Condensed Matter, 64*(2), 189-193.

Bilgili, Ö. (2021). Structural and electrical properties of nanosized Sm2O3 doped Bi1. 6Pb0. 4Sr2Ca2Cu3Oy superconductors. *Journal of Low Temperature Physics, 204*(5), 223-234.

de Vera, F. I., Bardolaza, H., Arcilla, C., & Sarmago, R. (2019). Effect of In2O3 on the grain connectivity and superconducting behavior of Bi2Sr2− x In x CaCu2O8+ d. *SN Applied Sciences, 1*(1), 96.

Frank, M., Frauenhofer, J., Van Hasselt, P., Nick, W., Neumueller, H.-W., & Nerowski, G. (2003). Long-term operational experience with first Siemens 400 kW HTS machine in diverse configurations. *IEEE Transactions on Applied Superconductivity, 13*(2), 2120-2123.

Guner, S., Zalaoglu, Y., Turgay, T., Ozyurt, O., Ulgen, A., Dogruer, M., & Yildirim, G. (2019). A detailed research for determination of Bi/Ga partial substitution effect in Bi-2212 superconducting matrix on crucial characteristic features. *Journal of Alloys and Compounds, 772*, 388-398.

Hernández-Wolpez, M., Gallart-Tauler, P., García-Fornaris, I., Govea-Alcaide, E., Pérez-Tijerina, E., Jardim, R. d. F., & Muné, P. (2020). Trapping of Magnetic Flux in Bi-2223 Ceramic Superconductors Doped with α-Al2 O 3

Nanoparticles. *Journal of Superconductivity and Novel Magnetism, 33*(3), 675-682.

Humaidi, S. (2020). *Development of TBCCO high temperature superconductor.* Paper presented at the AIP Conference Proceedings.

Kır, M. E., Özkurt, B., & Aytekin, M. E. (2016). The effect of K-na co-doping on the formation and particle size of Bi-2212 phase. *Physica B: Condensed Matter, 490*, 79-85.

Kocabas, K., Özkan, O., Bilgili, O., Kadıoglu, Y., & Yılmaz, H. (2010). The effects of Mg substitution in Bi-2223 superconductors. *Journal of Superconductivity and Novel Magnetism, 23*, 1485-1492.

Nurbaisyatul, E., Azhan, H., Kasim, A., & Ibrahim, N. (2020). Effect of CeO2 nanoparticle on the structural and electrical properties of BSCCO-2223 high temperature superconductor. *Solid State Phenomena, 307*, 104-109.

Özçelik, B., Ergin, I., Madre, M., & Sotelo, A. (2020). Effect of rubidium substitution on the physical and superconducting properties of textured high-Tc BSCCO samples. *Journal of Superconductivity and Novel Magnetism, 33*, 1285-1292.

Özkurt, B. (2012). Effects of Ni substitution in Bi-2212 superconductors. *Journal of Superconductivity and Novel Magnetism, 25*, 1775-1779.

Özkurt, B. (2014). Improvement of the critical current density in Bi-2223 ceramics by sodium–silver co-doping. *Journal of Materials Science: Materials in Electronics, 25*, 3295-3300.

ÖZTORNACI, U., & Özkurt, B. (2017). The effect of nano-sized metallic Au addition on structural and magnetic properties of Bi1. 8Sr2 AuxCa1. 1Cu2. 1Oy (Bi-2212) ceramics. *Ceramics International, 43*(5), 4545-4550.

Scalapino, D. J. (1995). The case for dx2− y2 pairing in the cuprate superconductors. *Physics Reports, 250*(6), 329-365.

Şakiroğlu, S., & Kocabaş, K. (2011). The Effect of Silver Substitution in Bi 1.7 Pb 0.3 Sr 2 Ca 2− x Ag x Cu 3 O y. *Journal of Superconductivity and Novel Magnetism, 24*, 1321-1325.

Tran, D. H., Pham, A. T., Le, T. M., Anh, D. T., Phan, Y. T., Man, N. K., . . . Kang, W.-N. (2019). Enhanced flux pinning properties in Bi 1.6 Pb 0.4 Sr 2− x K x Ca 2 Cu 3 O 10+ δ compounds. *Journal of Materials Science: Materials in Electronics, 30*, 8233-8238.

Tsuei, C., & Kirtley, J. (2000). Pairing symmetry in cuprate superconductors. *Reviews of Modern Physics, 72*(4), 969.

Ulgen, A., Turgay, T., Terzioglu, C., Yildirim, G., & Oz, M. (2018). Role of Bi/Tm substitution in Bi-2212 system on crystal structure quality, pair wave function and polaronic states. *Journal of Alloys and Compounds, 764*, 755-766.

Verma, P. K., Kaipamangalath, A., Varma, M. R., & Bai, V. S. (2023). Nonreactive Nano WO 3 Inclusions to Enhance Flux Pinning in Bi-2223 Superconductor Composites. *IEEE Transactions on Applied Superconductivity, 34*(1), 1-12.

Vu, L. H., Pham, A. T., Thien, N. D., Nam, N. H., Riviere, E., Pham, Q. N., . . . Nguyen, T. L. (2023). Enhancements of critical current density in Bi1. 6Pb0. 4Sr2Ca2Cu3O10+ δ superconductors by additions of SnO2 nanoparticles. *Ceramics International, 49*(16), 27614-27621.

Wang, T., Wang, W., & Wang, Y. (2023). Enhanced flux pinning properties for GdBa2Cu3O7− x films with nanosized La0. 67Sr0. 33MnO3 inclusions on SrTiO3 substrate by RF magnetic sputtering method. *Journal of Materials Science: Materials in Electronics, 34*(4), 257.

Yamauchi, H., & Karppinen, M. (1998). Hole-doping of the CuO2 planes in high Tc superconductors. *Materials Science and Engineering: B, 54*(1-2), 92-97.

Zelati, A., Amirabadizadeh, A., Kompany, A., Salamati, H., & Sonier, J. (2014). Effect of Eu 2 O 3 nanoparticles addition on structural and superconducting properties of BSCCO. *Journal of Superconductivity and Novel Magnetism, 27*, 1369-1379.

Zhang, S., Li, C., Hao, Q., Feng, J., Lu, T., & Zhang, P. (2015). Optimized intergrain connection and transport properties of Bi-2212 high-temperature superconductors by Ag nanoparticles inclusions. *Journal of Superconductivity and Novel Magnetism, 28*, 1729-1736.

Zhang, Z., Fang, Z., Zhou, M., Yang, D., Yu, M., Jin, H., . . . Li, C. (2024). The first CICC-type Bi-2212 insert coil for high-field applications up to 20 T. *Superconductor Science and Technology, 37*(12), 12LT01.

BİDGE